OPEN ACCESS
Journal of Multidisciplinary Applied Natural Science Vol. 6 No. 3 (2026) https://doi.org/10.47352/jmans.2774-3047.384
Check for updates
Research Article

Multiphase Nanoparticles from Eggshell Waste as Antibacterial Agents against Rice Blight in Lampung

Rodhiansyah Djayasinga, Wasinton Simanjuntak, Sumardi Sumardi, Sutopo Hadi, Mimi Sugiarti, Hartanti Hartanti, and Rudy Tahan Mangapul Situmeang*

Received : September 10, 2025	Revised : December 24, 2025	Accepted : April 13, 2026	Online : May 6, 2026

Abstract
This study reports the first isolation of an *Enterobacter cloacae complex* (ECC) strain, closely related to *Enterobacter hormaechei* (99.86% 16S rRNA identity), associated with bacterial blight symptoms in rice in Lampung, Indonesia. Acknowledging 16S rRNA limitations within ECC, species identification is reported cautiously, while pathogenicity profile fulfilled Modified Koch's Postulates. To address chemical bactericide limitations, we developed sustainable multiphase nanoparticles from chicken eggshell waste through mechanical and thermal decomposition approaches. The produced nanoparticles were characterized using XRD, TEM, FTIR, SEM-EDS, PSA, and UV-DRS. The results showed that the nanoparticles consisting of $Ca(OH)_2$, CaO, and β-tricalcium phosphate, with a dimension of 11–31 nm (XRD) and 20–23 nm (TEM). The FT-IR/EDS data confirmed OH^-, Ca, O, and P elements, while UV-DRS showed a bandgap energy of 5.96 eV. Descriptive statistical analysis (n=6) evaluated antibacterial activity via disk diffusion (20 µg/disk) against the ECC isolate, compared to ampicillin sulbactam (SAM 20). Nanoparticles yielded a mean inhibition zone of 10.06±0.02 mm for responsive replicates, demonstrating moderate activity. Within the zones, bacterial cells showed morphological damage, likely caused by Ca^{2+} and OH^- release, inducing membrane disruption and oxidative stress. Furthermore, spatially graded element distribution (Ca, O, P) and β-TCP as a controlled release matrix support sustained bioactivity. These findings reveal eggshell-derived nanoparticles as a promising, economical, and environmentally friendly antibacterial agent for sustainable rice disease management.

Keywords: chicken eggshell waste, *Enterobacter hormaechei*, environmentally friendly, multiphase nanoparticles, thermal decomposition

1. INTRODUCTION

Leaf blight disease, commonly caused by *Xanthomonas oryzae pv. oryzae*, leads to reduced rice production, which is a staple food for a significant portion of the world's population [1]. To address this challenge, various chemical methods have been used, including berberine, which disrupts cell membranes, reduces biofilm formation, and affects the energy metabolism of *Xanthomonas oryzae pv. oryzae* [2]. Silver nanoparticles have been reported to inhibit the growth of *Xanthomonas oryzae pv. oryzae* (Xoo) with an inhibition zone of 16.5 mm [3]. Chiral axial thiazine molecules at a concentration with an EC_{50} value of 4.18 µg/mL show inhibitory activity against Xoo as well [4]. Furthermore, 2-quinazolin-4-ones show inhibitory potential by altering bacterial morphology and increasing reactive oxygen species, which disrupt growth and motility [5]. The biopesticide 3,4-dimethoxyphenol on Xoo causes the cells to show surface depression, wrinkles, and distortion, leading to cell lysis [6]. Chemical treatment has faced various weaknesses such as resistance depending on bacterial strains, shifts in the pathogenicity pattern of Xoo, adaptation potential, and proliferation in resource-limited environments [7].

However, several studies have reported that *Enterobacter*, a genus traditionally associated with environmental and clinical settings is increasingly implicated in phytopathogenic roles in rice, with documented infections in Korea, India, and China [8]–[10]. The ability of *Enterobacter* to cause bacterial blight is attributed to its capacity to produce copious amounts of exopolysaccharides (EPS), a trait commonly associated with virulence in plant-pathogenic bacteria. EPS facilitates host colonization, confers protection against environmental stresses, and contributes to the occlusion of host vascular tissues [11]. In contrast to well-established rice pathogens such as Xoo which rely on the production of cell wall-degrading enzymes (CWDEs) for tissue invasion and maceration, *Enterobacter* strains exhibit markedly reduced or negligible CWDE activity. Despite this

Table 1. Nanoparticles crystal structure of calcined chicken eggshell powder.

Crystal phase	Lattice Structure	Space group	Cell Parameters	Characteristic peaks (2θ)	Ref.
Calcium oxide (CaO)	cubic	Fm3m	a = 4.81 Å	32.2°, 37.4°, 53.9°, 64.2°, 67.4°, 79.6°, 88.5°	[21]
Calcium hydroxide ($Ca(OH)_2$)	Hexagonal	P3m1	a = 3.59 Å, c = 4.91 Å	18.1°, 28.7°, 34.1°, 47.1°, 50.8°, 54.3°, 62.6°	[22]
Calcite ($CaCO_3$)	Trigonal	R3c	a = 4.99 Å, c = 17.06 Å	23.1°, 29.4°, 31.4°, 35.9°, 39.4°, 43.2°, 47.5°, 48.5°, 49.0°, 56.0°, 57.4°, 60.6°, 62.6°, 64.4°, 65.4°	[23]
Vaterite ($CaCO_3$)	Hexagonal	P63/mmc	a = 7.14 Å, c = 16.93 Å	20.9°, 24.9°, 27.1°, 32.7°, 33.1°, 43.9°, 49.0°, 50.0°, 55.9°, 56.6°	[24]
Calcium phosphate ($Ca_3(PO_4)_2$)	Rhombohedral	R3c	a = 10.43 Å, c = 37.38 Å	26.0°, 30.7°, 34.2°, 46.5°	[25]
Magnesium calcite ($Ca_{0.94}Mg_{0.06}O_3$)	Trigonal	R3c	a = 4.99 Å, c = 17.06 Å	23.3°, 29.6°, 31.6°, 36.1°, 39.6°, 43.4°, 47.7°, 48.7°, 49.2°, 56.2°, 57.6°, 60.8°, 62.8°, 64.6°, 65.6°	[26] - [28]
Hydroxyapatite ($Ca_{10}H_2O_{26}P_6$)	Hexagonal	P63/m	a = 9.42 Å, c = 6.88 Å	25.9°, 28.0°, 28.9°, 31.7°, 32.2°, 32.9°, 34.0°, 39.8°, 46.7°, 49.5°, 50.5°, 53.1°, 53.9°	[29] [30]

distinct pathogenic strategy, the role of environmental and agronomic factors in driving the emergence of Enterobacter-associated bacterial blight in rice remains unexplored [12]. Recently, we detected ECC isolate (cf. *Enterobacter hormaechei*) a species not previously linked to rice blight in Indonesia causing bacterial leaf blight in rice plants in Haduyang Village, Natar District, South Lampung Regency. Control measures against this emerging pathogen are currently unavailable. Given the limitations of conventional chemical bactericides, sustainable alternatives are urgently needed [13].

Chicken eggshell waste, with its high calcium content, porous architecture, and abundance as an agro-industrial byproduct, offers a promising, low-cost, and eco-friendly material [14]. Our prior work has demonstrated its antibacterial potential [15], providing the foundation for developing eggshell-derived nanoparticles as a novel intervention against both classical and emerging rice blight agents. Green nanotechnology enables the synthesis of biomass waste-derived nanoparticles such as those from eggshells as sustainable and effective antibacterial agents, with promising applications in plant disease management [16]. The importance of chicken eggshell powder in materials science has gained significant attention due to its potential as a sustainable antibacterial agent [17]. As an abundant agro-industrial by product approximately 150,000

tons of eggshells are discarded annually in Indonesia alone, its valorization aligns with the principles of the circular economy, which emphasizes waste-to-resource transformation, closed loop systems, and reduction of environmental burdens [18][19].

By converting this low-value waste into functional multiphase nanoparticles, our approach embodies green nanotechnology as it employs solvent-free, energy-efficient thermal and mechanical processing without toxic reagents, minimizes secondary waste, and leverages naturally occurring biocompatible compounds such as calcium and phosphate [20]. Previous studies [21]-[30] have analyzed the crystal phase structures of calcined chicken eggshell powder, identifying components including calcium oxide, calcium hydroxide, calcite, vaterite, calcium phosphate, hydroxyapatite, and magnesium calcite phases whose synergistic interactions may enhance antibacterial efficacy (Table 1).

Based on previous research, knowledge on the use of calcined chicken eggshell powder as an antibacterial agent against bacterial blight is still limited. However, considering the advantages of calcined chicken eggshell powder, such as its high CaO content, biocompatibility, abundance as poultry farming waste, and potential for sustainable material valorization. Therefore, this study aims to comprehensively characterize the crystal structure, surface morphology, and optical properties of multiphase nanomaterials synthesized through an eco-friendly and low-energy process from chicken eggshell powder, and to assess their potential as an antibacterial agent specifically targeting *Enterobacter* spp. responsible for bacterial blight in rice.

2. MATERIALS AND METHODS

2.1. Materials

Chicken eggshell was collected from household waste in Bandar Lampung City, Indonesia. The material was washed, and ground using a porcelain mortar through a top-down method. In this study, the processing of these materials did not include the use of any chemical substances. To test the potential antibacterial activity of the synthesized material; antibiotics ampicillin sulbactam 20 µg (Oxoid), nutreint agar plate (NAP, Merck), Mueller Hinton agar (MHA, Oxoid), MacConkey agar (MC, Merck), and brain heart infusion broth (BHIB, Merck) culture were used, followed by Gram staining. Suspect bacteria samples were obtained from the isolates originating from rice plant belonging to the community that were attacked by bacteria blight disease located in Haduyang Village, Natar District, South Lampung Regency, Indonesia.

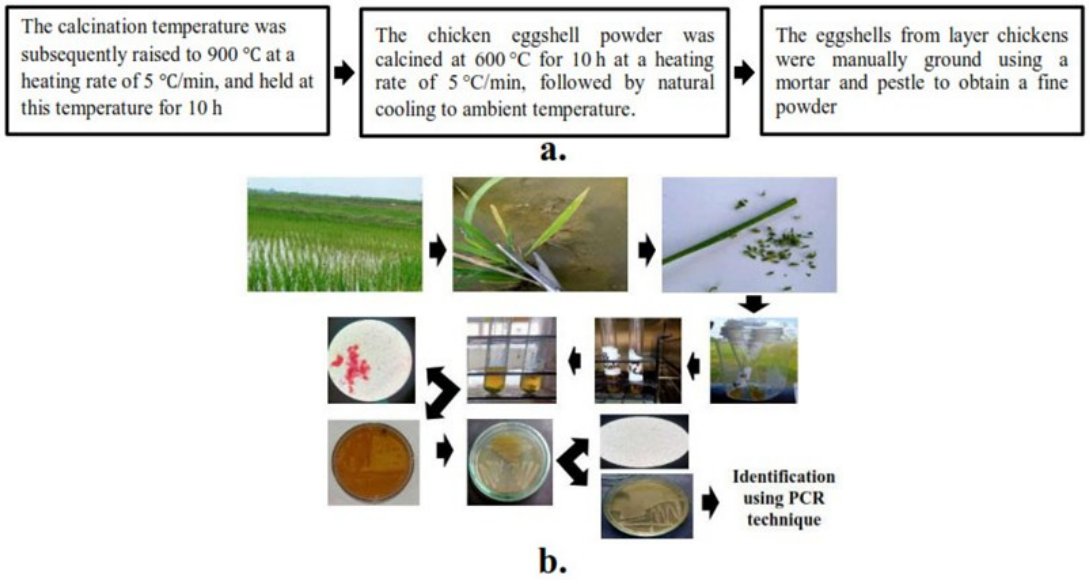

Figure 1. (a) Schematic of multiphase nanoparticles synthesis and (b) workflow for isolating putative bacterial blight pathogens from symptomatic rice plants.

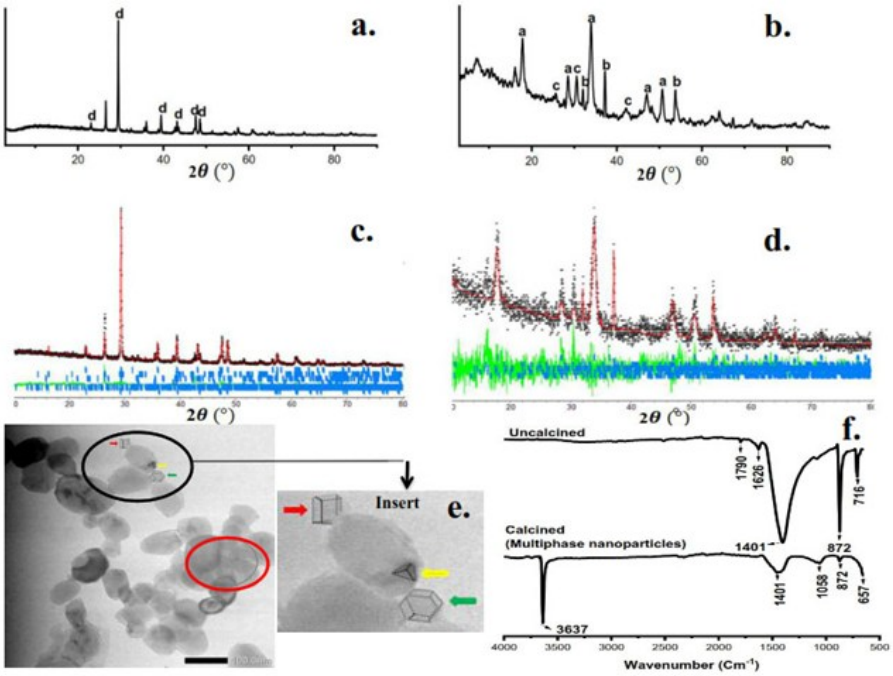

Figure 2. Characterization of eggshell-derived materials: (a,b) XRD of uncalcined eggshell [28], and calcined eggshell–derived multiphase nanoparticles; (c,d) Rietveld-refined phase quantification; (e) TEM image (100 nm scale bar) showing crystalline domains; (f) FT-IR spectra of uncalcined [28], and multiphase nanoparticles.

2.2. Methods

2.2.1. Synthesis of Multiphase Nanoparticles

This study was conducted from September 2024 to March 2025 at the Laboratory of Chemistry and Bacteriology of the Medical Laboratory Technology Department, Faculty of Medical Laboratory Technology, Tanjungkarang Health Polytechnic, Bandar Lampung, Indonesia. Subsequently, bacterial isolates were inoculated into a series of selective and non-selective culture media to optimize growth conditions and ensure phenotypic stability, thereby enhancing the reliability of subsequent antimicrobial assays without compromising the integrity of modified purification protocols.

Based on the previous report, the synthesis of multiphase nanoparticles through the processing of chicken eggshell waste included the initial step of grinding using a porcelain mortar to obtain a fine, homogenous powder, as shown in Fig. 1(a). It followed by calcination using Lenton UAF 16/10 furnace instrumentation with a controlled heating ramp of 5 °C/min up to 600 °C, held isothermally for 10 h [31]. This constituted the first calcination stage and was succeeded by a second stage involving a further ramp of 5 °C/min to 900 °C, maintained for 10 h under static air atmosphere to promote complete phase transformation and crystallite growth [28][29].

2.2.2. Isolation and Identification of Suspect Bacteria

Bacterial isolation was performed according to the workflow illustrated in Fig. 1(b), with modifications based on established protocols [32] [33]. Leaf samples exhibiting typical symptoms of bacterial leaf blight characterized by yellowing along the leaf margins were collected from infected rice plants in Lampung. The symptomatic tissue was aseptically excised, cut into small fragments (~5 mm), and transferred into nutrient broth, followed by incubation at 37 °C for 24 h to enrich potential pathogens.

To selectively isolate Gram-negative bacteria particularly members of the *Enterobacteriaceae* family, which include common plant-associated pathogens such as *Xanthomonas spp*. the enriched culture was streaked onto MacConkey agar. This differential and selective medium inhibits Gram-

positive bacteria while allowing Gram-negative isolates to grow lactose-fermenting strains produce pink colonies, whereas non-fermenters (including many *Xanthomonas* species) form colorless or pale colonies. Although *Xanthomonas oryzae pv. oryzae* is typically nonlactose fermenting, preliminary observations in our study indicated that certain environmental isolates from blighted rice leaves exhibited atypical colony morphologies on MC, necessitating a secondary selection step [34].

Distinct colonies from MC were then subcultured onto NAP to support robust growth and facilitate phenotypic characterization [35]. Among the resulting isolates, those producing a characteristic yellow pigment a trait commonly associated with *Xanthomonas* species due to xanthomonadin production were prioritized as putative causal agents of bacterial leaf blight. These yellow-pigmented colonies were subjected to Gram staining (expected to be Gram-negative rods) and purified through repeated streaking on NAP to obtain axenic cultures for subsequent molecular and pathogenicity assays [36]. To ensure culture purity, single-colony isolation was performed via repeated streaking on NAP until uniform colony morphology was achieved. The same isolate code ('Djayasinga') was consistently employed across all downstream analyses, including 16S rRNA sequencing, pathogenicity assays, antibacterial evaluations, and SEM-EDS characterization.

For the identification process, the bacterial isolate was submitted to the Genetic Testing Laboratory of Science Indonesia. Based on our initial hypothesis that the pathogen was Xoo, we

Table 2. Crystal structure of nanoparticles multiphase.

Crystal Phases (Lattice)	Space group	Atoms	Atom position coordinates		
			x	y	z
$Ca(OH)_2$ (Hexagonal)	P -3 M1	Ca	0.00000	0.00000	0.00000
		O	0.30000	0.60000	0.70000
		H	0.30000	0.60000	0.50000
CaO (Cubic)	F M 3 M	Ca	0.00000	0.00000	0.00000
		O	0.50000	0.50000	0.50000
β-TCP ($Ca_3(PO_4)_2$) (Trigonal)	F 3 C H	Ca 1	0.72590	0.86180	0.16630
		Ca 2	0.61880	0.82550	-0.03320
		Ca 3	0.72660	0.85140	0.06110
		Ca 4	0.00000	0.00000	-0.08510
		Ca 5	0.00000	0.00000	0.73360
		P 1	0.00000	0.00000	0.00000
		P 2	0.68720	0.86060	0.86060
		P 3	0.65300	0.84640	0.76680
		O 1	0.72560	-0.09440	-0.09170
		O 2	0.76740	0.78330	0.85480
		O 3	0.72980	0.00880	0.84860
		O 4	0.52210	0.76080	0.86270
		O 5	0.59870	-0.04880	0.77940
		O 6	0.00570	0.69300	0.78500
		O 7	0.08030	0.89900	0.77710
		O 8	0.63200	0.82580	0.72680
		O 9	0.00570	0.86240	-0.01150
		O 10	0.00000	0.00000	0.04210

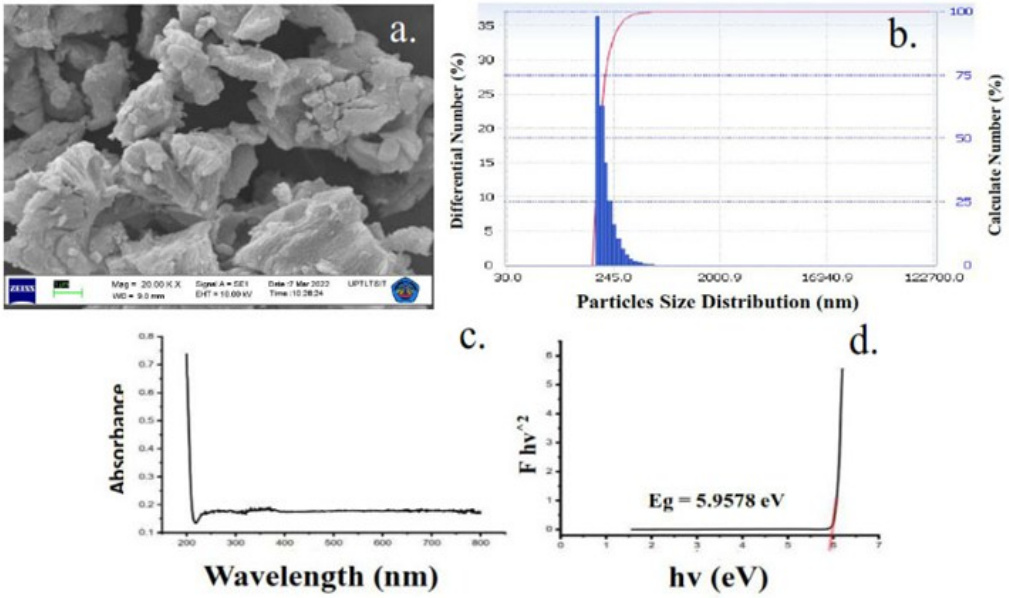

Figure 3. (a) SEM image of multiphase nanoparticles (20,000×; scale bar: 1 µm); (b) particle size distribution from analyzer; (c) UV–vis spectrum and (d) corresponding Tauc plot for bandgap determination.

employed a specific primer set, XOR-F (5′-GCATGACGTCATCGTCCTGT-3′)XOR-R2 (5′-CTCGGAGCTAATGCCGTGC-3′), for DNA amplification [37]. Nonetheless, PCR analysis failed to produce an amplicon corresponding to Xoo. Consequently, further identification was performed using 16S rRNA gene sequencing [38].

The 16S rRNA gene was amplified using the MyTaq HS Red Mix, 2X (Bioline, BIO-25048). The concentration and purity of the extracted DNA were determined using a NanoDrop 2000 spectrophotometer Amplified products were verified by agarose gel electrophoresis. Bidirectional sequencing was subsequently performed using the Sanger sequencing method with capillary electrophoresis to obtain accurate nucleotide reads. The sequence data were then processed and refined through bioinformatics analysis as described in, producing consensus sequences for further interpretation [39][40].

2.2.3. Pathogenicity Test

To confirm the pathogenicity of the ECC isolate (cf. *E. hormaechei*) that had been molecularly identified, a leaf dip inoculation assay was performed on healthy rice leaves [41]. Bacterial cultures were grown in BHIB for 24 h at 37°C with shaking at 150 rpm. The bacterial suspension was adjusted to an optical density of OD_{600} prior to inoculation. Fresh wound sites were created by cutting 3 cm from the leaf tips using sterile scissors. The cut ends were immersed in the bacterial suspension for 5 min and subsequently incubated under ambient laboratory conditions. Sterile BHIB and an *Escherichia coli* suspension (non-phytopathogenic control) served as negative controls. Disease development was monitored daily for 6 days. Symptoms were photographically documented to visually confirm the occurrence of chlorosis and necrosis [42].

2.2.4. Evaluation of Antibacterial Activity

The antibacterial assay was performed using the Kirby-Bauer disk diffusion method. The bacterial suspension of the ECC isolate (cf. *E. hormaechei*) was adjusted to a 0.5 McFarland turbidity standard and uniformly inoculated onto the surface of MHA using a sterile cotton swab. Plates were allowed to stand for 15 min prior to disk placement [43]. A small amount of synthesized multiphase nanomaterial powder was placed on the surface of the MHA culture, with all procedures performed in the BSC room. All bacteria plates were incubated at 37 °C for 24 h using an incubator [44]. Observations of the incubation results were carried out on the emergence of inhibition zones for the growth of *ECC* (cf. *E. hormaechei*) bacteria using

scanning electron microscopy-energy dispersive X-ray spectroscopy (SEM-EDS) instrumentation on bacteria cells damaged by intervention from multiphase nanoparticles.

The pH measurements were conducted using calibrated universal pH indicator paper (range 1-144, Merck KGaA, Germany) with a resolution of ±0.5 pH units. Three distinct measurements were performed; (1) Nanoparticle suspension pH: A stock suspension was prepared by dispersing 50 mg of multiphase nanoparticles in 50 mL of sterile distilled water (solid-to-liquid ratio: 1 mg/mL), followed by sonication for 10 min to ensure homogeneity. The pH was measured after 5 min of contact time by immersing the pH paper into the suspension; (2) MHA medium pH: The pH of uninoculated Mueller-Hinton Agar was measured by gently placing the pH paper on the agar surface for 30 s prior to bacterial inoculation; (3) Inhibition zone pH: Post-incubation (24 h at 37°C), the pH within the clear inhibition zone was measured by placing the pH paper directly on the agar surface at the zone center for 30 s. Color changes were compared against the manufacturer's reference chart under standardized lighting conditions [45].

2.2.5. Statistical Analysis

The evaluation of the antibacterial activity of multiphase nanoparticles was conducted using the Kirby-Bauer disk diffusion method with a standardized experimental design. The preparation of the bacterial suspension for the ECC isolate (cf. *E. hormaechei*) followed the procedure. Six sterile paper disks, each impregnated with 20 µg of multiphase nanoparticles (20 µg/disk, n = 6), were aseptically placed on a single MHA plate inoculated with the bacteria. As a positive control, Ampicillin Sulbactam (SAM 20) was placed on a separate MHA plate with identical bacterial inoculation preparation. All treatments were incubated at 37 °C for 24 hours. Inhibition zone data obtained from six independent replicates (n = 6) were analyzed using descriptive statistics to calculate mean, standard deviation (SD), median, and data range. Antibacterial response rate was expressed as the percentage of replicates showing positive inhibition zones (>0 mm) [46].

The minimum inhibitory concentration (MIC) of multiphase nanoparticles against ECC isolate (cf. *E. hormaechei*) was determined using the broth microdilution method. Briefly, a stock suspension of multiphase nanoparticles was prepared by dispersing 50 mg of the material into 50 mL of sterile distilled water (concentration 1000 µg/mL) via sonication. Two-fold serial dilutions were performed in test tubes to obtain test concentrations ranging from 100, 50, 20, 10, 5, 2 µg/mL. Each test tubes containing 100 µL of nanoparticle suspension was inoculated with 100 µL of standardized bacterial suspension (adjusted to 0.5 McFarland standard and diluted 1:100 in BHIB to achieve a final inoculum of ~5 × 10^5 CFU/mL). Positive growth controls (bacteria without nanoparticles) and negative sterility controls (media without inoculum) were included in parallel. The plates were incubated at 37 °C for 24 h. Bacterial growth was assessed visually based on turbidity [47].

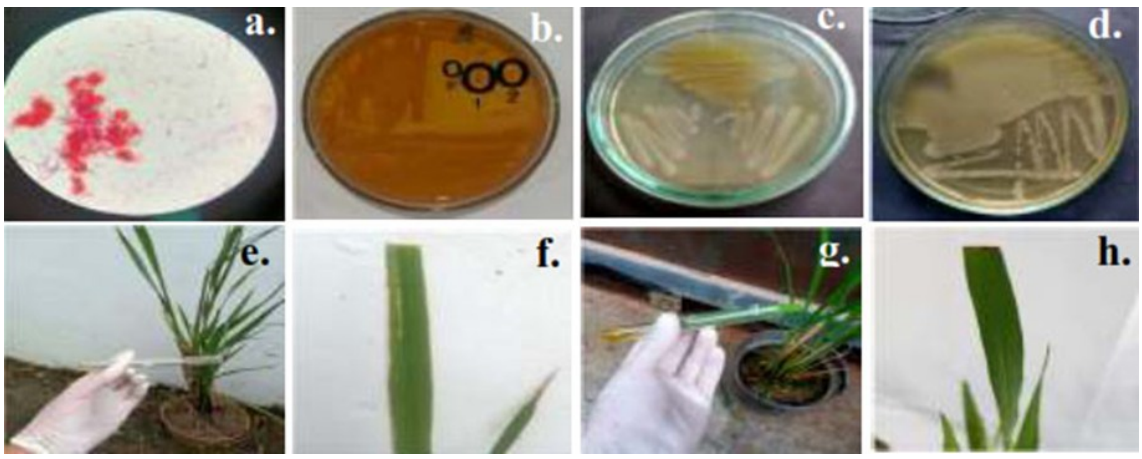

Figure 4. (a–d) Morphology of bacterial isolates from blight-symptomatic rice plants. (e–f) pathogenicity test using ECC (cf. *Enterobacter hormaechei)* isolate, and (g-h) using *Escherichia coli*.

Table 3. DNA quantification, and purification.

Sample code	Consentration (ng/ µL)	$A_{260/280}$	$A_{260/230}$	Volume (µL)
Djayasinga	177.9	1.93	2.23	35

3. RESULTS AND DISCUSSIONS

3.1. XRD Analysis

The non-calcined, and calcined eggshell powders (multiphase nanoparticles) were analyzed using a Shimadzu XRD-6000 diffractometer. Qualitatively, the characteristic diffraction peaks (2θ) of both materials are presented in Fig. 2. The three dominant peaks at 2θ°, 23.22° hkl (012), 29.49° hkl (104), and 39.62° hkl (113) as shown by the letter "d" in Fig. 3(a), represented the crystalline phase of calcite ($CaCO_3$) present in the uncalcined eggshell powder. This peak showed similarity with the results of previous studies which had the ID COD-9009668 [48].

The results of qualitative analysis of XRD data on multiphase nanoparticles were shown with the letter "a" in Fig. 2(b) for three dominant peaks at 2θ°, 17.82°, 28.54°, and 33.94°. These peaks were identical to the $Ca(OH)_2$ crystal phase with the highest intensity at 33.92° hkl (011), as referred to in the previous reference with ID COD-0000117 [49]. Letter "b" in Fig. 2(b) represented the CaO crystal phase with identical peaks at 2θ°, 32.04°, 37.22°, and 53.78° with the highest peak intensity at 37.22° hkl (221) which resembled the reference peak from previous studies [50]. The peaks at 21.80°, 31.00°, and 34.11° with the highest intensity at 34.34° hkl (220) are the crystalline phase of beta-tricalcium phosphate $Ca_3(PO_4)_2$, marked with the letter "c" in Fig. 2(b), according to previous studies with ID COD-1517238 [51].

The results of quantitative analysis using the Rietica method version 4.2 Rietveld [52], obtained results in the form of a comparison of the diffractograms of non-calcined, and multiphase nanoparticles (calcined), as shown in Fig. 2(c), and 2(d). In addition to the diffractogram image, the goodness of fit (GoF) values for both samples were 2.61, and 1.509, respectively, which were close to the standard GoF value, namely <4 [53]. In Rietveld refinement, a GoF value below 4 is generally considered acceptable, as it indicates a reasonable agreement between the observed and calculated diffraction patterns, accounting for typical experimental imperfections such as minor impurities, microstructural effects, or instrumental broadening [54]. Characterization showed that the $Ca(OH)_2$ crystal lattice had a hexagonal structure with defined cell parameters (a = 3.5890 Å c = 4.9095 Å), angles ($\alpha = \beta = 90°$, $\gamma = 120°$), and cell volume of 639.8533. Additionally, the unit cell contained a single formula unit (Z = 1), and the atomic positions of calcium, oxygen, and hydrogen were at specific coordinates (x = 0 (Ca), x = 0.3 (O and H); y = 0 (Ca), y = 0.6 (O and H); z = 0 (Ca), z = 0.7 (O), z = 0.5 (H). The information on the crystal lattice structure of CaO showed cubic shape, cell parameters (a = 4.80920 Å, angles ($\alpha = \beta = \gamma = 90°$), a unit cell containing four units (Z = 4), and cell volume of 111.217003. Additionally, information was obtained on the crystal lattice structure of β-Tricalcium phosphate (β-TCP ($Ca_3(PO_4)_2$). This included trigonal, cell parameters (a = 10,48520 Å; c = 37,25870 Å), angles ($\alpha = \beta = 90°$, $\gamma = 120°$), unit cell containing 21 units (Z = 21), and cell volume of 3546.496582. The coordinate positions of the atoms of the crystal phases $Ca(OH)_2$, CaO, beta-Tricalcium phosphate (β-TCP ($Ca_3(PO_4)_2$ are shown in Table 2.

The full width half maximum (FWHM) value of the $Ca(OH)_2$ crystal phase is 0.74 with the Weight Percentage of Phase information of 57.25. By entering the FWHM value with a 2θ angle of 33.94° which is the peak with the highest intensity of the $Ca(OH)_2$ crystal phase into the Debye-Scherrer equation, the size of $Ca(OH)_2$ nanoparticles crystal phase is obtained as 11.23 nm. Meanwhile, the Weight Percentage of Phase CaO, β-TCP ($Ca_3(PO_4)_2$) is 10.34, and 4.7 respectively. The size information of CaO crystal phase is 31.07 nm obtained by performing calculations including the FWHM value of 0.27 at the peak intensity of 2θ 37.22°. Additionally, the size information of the β-TCP ($Ca_3(PO_4)_2$) crystal phase is obtained at 23.11 nm by calculating the FWHM value of 0.36 and the peak intensity at 2θ 34.34°.

The thermal decomposition of eggshell primarily composed of calcite ($CaCO_3$) typically initiates around 600 °C due to the presence of a native organic matrix and approaches completion near 900 °C under ambient atmosphere [55]. In this work, eggshell powder was first calcined at 600 °C for 10 h, inducing partial decomposition of $CaCO_3$ into CaO, as evidenced by the reduction of calcite diffraction peaks. The sample was then cooled to room temperature and subjected to a second calcination at 900 °C for 10 h to ensure complete removal of residual carbonate and organic matter. During the subsequent cooling phase in ambient air, the highly reactive CaO surface partially hydrated to form $Ca(OH)_2$ [56]. Quantitative Rietveld refinement of XRD data confirmed the presence of three crystalline phases: $Ca(OH)_2$ (57.25 ± 1.2 wt%), CaO (10.34 ± 0.8 wt%), and β-tricalcium phosphate (β-TCP, 4.70 ± 0.5 wt%). The remaining ~27.71 wt% is attributed to amorphous content and/or minor crystalline phases below the detection limit of XRD (~2–5 wt%). This amorphous fraction is consistent with the mechanical-thermal decomposition synthesis route, which can generate non-crystalline calcium carbonate residues or disordered surface layers on nanoparticle surfaces [57].

The presence of *β*-TCP is attributed to trace phosphorus originating from phosphoproteins naturally embedded in the eggshell's organic matrix, which, under prolonged high-temperature treatment, transformed into PO_4^{3-} groups and reacted with Ca^{2+} to nucleate *β*-TCP [58]. This assignment is further supported by TEM imaging, which revealed hexagonal morphology for $Ca(OH)_2$, cubic for CaO, and trigonal for *β*-TCP consistent with their respective crystal structures. Critically, this synthesis involves only eggshell waste and thermal treatment, without any external chemical additives, aligning with green nanotechnology principles [59].

3.2. TEM Analysis

TEM images were obtained by analyzing the multiphase nanoparticles material using a JEOL JEM-1400. Fig. 2(e) reveals that the calcined chicken eggshell powder consists of a multiphase crystalline nanoparticles assembly. Black circular insets highlight distinct crystalline phases, each exhibiting characteristic nanoparticle morphologies associated with their respective crystal structures. The hexagonal lattice characteristic of $Ca(OH)_2$ is

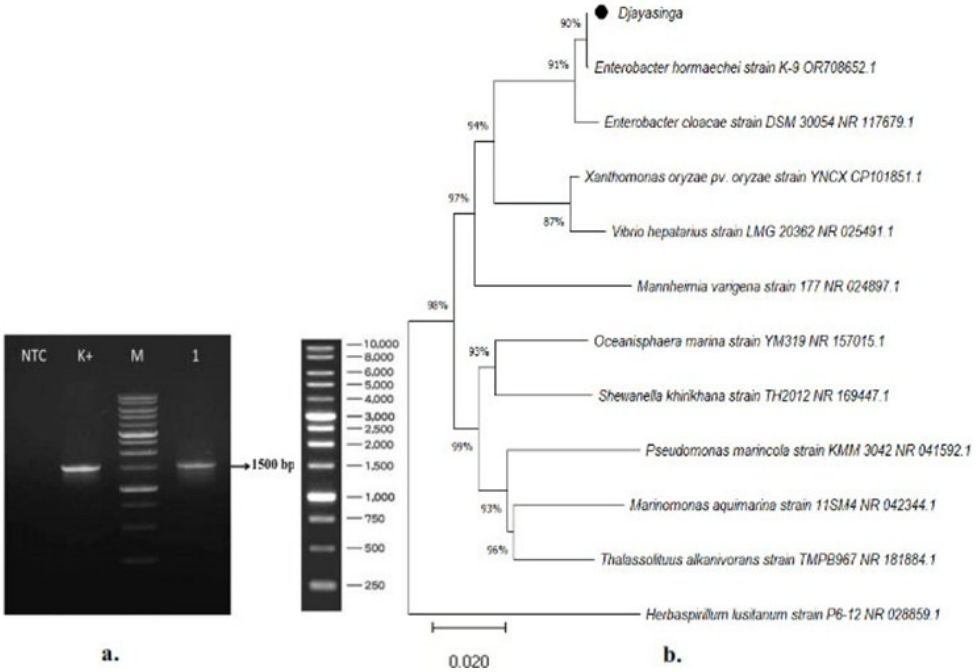

Figure 5. Molecular identification, and phylogeny of isolate Djayasinga. (a) 16S rRNA amplicons on agarose gel: NTC (No-Template Control), K+ (*E. coli* ATCC 25922), M (1 kb ladder); (b) Maximum-likelihood tree placing Djayasinga isolate in the *Enterobacter cloacae* complex, closest to ECC (cf. *E. hormaechei)* reference strains (16S rRNA analysis).

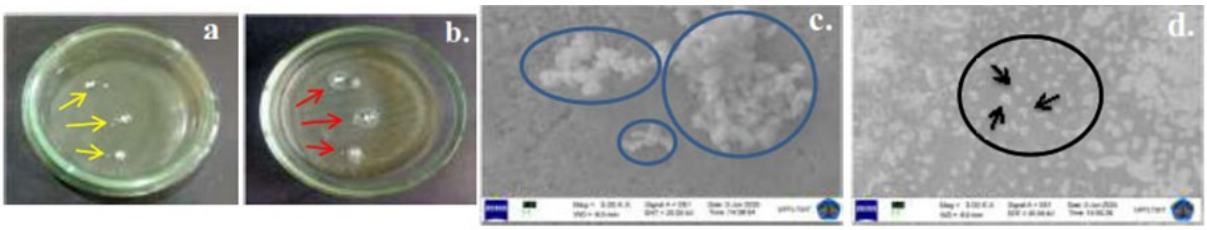

Figure 6. Antibacterial assessment of eggshell-derived multiphase nanoparticles against ECC (cf. *Enterobacter hormaechei*): (a) Kirby–Bauer assay setup; (b) inhibition zone; (c) SEM of untreated Ec cells; (d) SEM showing nanoparticle-induced morphological damage.

clearly identifiable, as indicated by green arrows. Red arrows denote regions exhibiting cubic symmetry, corresponding to the CaO phase. The trigonal structure of $Ca_3(PO_4)_2$ is indicated by the yellow arrow marking the γ angle of 120°, thus confirming the trigonal crystal system [60]. Due to phase intergrowth and stacking, certain regions exhibit overlapping diffraction contrasts, making phase discrimination challenging as circled in red circle for reference. The crystallite size of the CaO phase, as measured directly from TEM micrographs using digital calipers, is determined to be 20.55 nm. This value deviates significantly from the Scherrer equation-based calculation (11.23 nm), which derives crystallite dimensions from XRD peaks broadening. The discrepancy arises because TEM measurements reflect the actual physical grain dimensions, whereas the Scherrer method estimates the coherently diffracting domain size, typically corresponding to the dimension of a single crystalline unit or sub-grain within a polycrystalline aggregate [61]. A similar trend is observed for the $Ca(OH)_2$, and $Ca_3(PO_4)_2$ phases within the multiphase nanoparticles material, indicating that grain agglomeration and polycrystallinity contribute to the systematic overestimation of crystallite size in direct TEM analysis relative to XRD-based calculations.

3.3. FT-IR Analysis

This analysis was carried out using an Agilent Technologies Cary 630 FT-IR spectrometer. As shown in Fig. 2(f), the main absorption bands in the FTIR spectrum closely match the reference peaks for calcite ($CaCO_3$), and $Ca(OH)_2$. The broad O–H stretching band near 3640 cm^{-1} matches the characteristic peak of $Ca(OH)_2$ [62][63]. The asymmetric CO_3^{2-} stretching vibration at 1401 cm^{-1}, and the out-of-plane bending mode at 872 cm^{-1} are consistent with those reported for calcite [64][65]. The band at 716, and 675 cm^{-1}, attributed to Ca–O lattice vibrations, corresponds to modes previously reported in both experimental and theoretical studies of CaO-derived phases [66].

3.4. SEM Analysis

The multiphase nanoparticle material was analyzed by SEM using a Zeiss EVO MA10 SEM-EDS instrument. Fig. 3(a) presents SEM analysis showing that calcination of chicken eggshell powder at high temperatures induces particle agglomeration due to increased surface energy, which drives particle binding to minimize thermodynamic instability. This can be mitigated by mechanical or wet ball milling, reducing particle size and disrupting agglomerates [67]. The resulting porous morphology stems from CO_2 release during $CaCO_3$ decomposition at 900 °C, forming CaO, which hydrates to calcium hydroxide. Concurrently, elevated temperatures soften materials lowering Young's modulus, yield strength, and promote grain boundary mediated deformation, such as sliding and diffusion. In contrast, lower temperatures suppress dislocation activity, rendering grain boundary migration critical for plastic deformation [68].

3.5. Particle Size Distribution Analysis

The particle size distribution of the multiphase nanoparticles material was analyzed using a Beckman Coulter Particle Size Analyzer. The measurement conditions for particle distribution analysis were carried out at a temperature of 25 °C, using water as a dispersant, with a refractive index of 1.3328, a viscosity of 0.8878, and a scattering intensity of 11345. As shown in Fig. 3(b), the size distribution analysis of the calcined eggshell

Table 4. Top 10 Hit BLAST results against National Center for Bitechnology Information (NCBI), excluding uncultured sample sequences.

Isolate code	Result link				
	Description	**Maximum score**	**Total score**	**Percentage identity**	**Accession**
Djayasinga	*Enterobacter hormaechi* strain K-9 16S rRNA gene partial sequence	2564	2564	99.86%	OR708652.1
	Enterobacter hormaechi strain FF26 16S rRNA gene partial sequence	2564	2564	99.86%	KR778812.1
	Bacterium strain BS 1814 16S rRNA gene partial sequence	2558	2558	99.78%	MK825002.1
	Enterobacter sp. Strain FF20 16S rRNA gene partial sequence	2558	2558	99.78%	KR778810.1
	Enterobacter sp.strain FF18 16S rRNA gene partial sequence	2558	2558	99.78%	KR778809.1
	Enterobacter hormaechi strain FF3 16S rRNA gene partial sequence	2558	2558	99.78%	KR778805.1
	Enterobacter hormaechi strain CZW018 16S rRNA gene partial sequence	2558	2558	99.78%	MW435394.1
	Enterobacter sp. strain WA14-2-10 16S rRNA gene partial sequence	2556	2556	99.86%	MH341954.1
	Enterobacter sp. strain RCB253 16sSrRNA gene partial sequence	2555	2555	99.71%	KT260465.1
	Enterobacter sp. strain MY3 16S rRNA gene partial sequence	2553	2553	99.71%	MN894537.1
	https://www.ncbi.nlm.nih.gov/nuccore/ OR708652.1,KR778812.1,MK825002.1,KR778810.1,KR778809.1,KR778805.1,MW435394.1,MH341954.1,KT260465.1,MN894537.1 Limitation to *Xanthomonas*				
	Description	**Maximum score**	**Total score**	**Percentage identity**	**Accession**
	Xanthomonas oryzae pv. oryzae strain YNCX plasmid pYNCX4 complete sequence	1938	1938	92.55%	CP101851.1
	Xanthomonas oryzae pv. oryzicola strain YLA2-20 16S rRNA gene partial sequence	1376	1376	84.61%	OP684244.1
	Xanthomonas oryzae pv. oryzicola strain GAN2-2 16S rRNA gene partial sequence	1376	1376	84.61%	OP684243.1
	Xanthomonas oryzae pv. oryzicola strain D-9 chromosome complete genome	1373	2746	84.55%	CP045912.1
	Xanthomonas oryzae pv. oryzicola strain BA17 chromosome	1373	2746	84.55%	CP191182.1
	Xanthomonas oryzae pv. oryzicola strain BA16 chromosome	1373	2746	84.55%	CP191183.1
	Xanthomonas oryzae strain BA1118 chromosome	1373	2746	84.55%	CP191181.1
	Xanthomonas oryzae pv. oryzicola strain MA123 chromosome	1373	2746	84.55%	CP191180.1
	Xanthomonas oryzae pv. oryzicola strain MA135 chromosome	1373	2746	84.55%	CP191179.1
	Xanthomonas oryzae pv. oryzicola strain MD-P13-1-7 chromosome	1373	2746	84.55%	CP191178.1
	https://www.ncbi.nlm.nih.gov/nuccore/ CP101851.1,OP684244.1,OP684243.1,CP045912,CP191182.1,CP191183.1,CP191181.1,CP191180.1,CP191179.1,CP191178.1				

powder ranged from 175 to 289 nm, with the size of 245 nm being 50% more dominant. The particle size distribution is relatively larger than the size known from XRD and TEM analysis due to the agglomeration mechanism in the calcined powder. The calcination process produced a variety of crystal phases due to the thermal decomposition of calcium carbonate in the eggshell. During this process, the calcium carbonate in the eggshell decomposes into calcium oxide, which reacts with water. This causes van der Waals forces to form between surface particles, which induce agglomeration, resulting in a relatively large and diverse particle size distribution in the observed samples [69]–[71].

The reported hydrodynamic size reflects the as-dispersed agglomerated state in the absence of post synthesis deagglomeration. Future work could employ post-processing methods such as ultrasonication or ball milling to disrupt these agglomerates, reduce the effective particle size, and enhance colloidal dispersion, thereby better aligning the PSA results with the primary crystallite dimensions observed by XRD and TEM. Such approaches are particularly relevant for applications demanding high specific surface area and uniform nanoparticle distribution, including catalysis, environmental remediation, and nanocomposite fabrication [70][71].

Uniform grain growth arises under conditions of homogeneous grain boundary mobility, which is typically achieved when the material exhibits a narrow initial grain size distribution, uniform grain boundary energy, and the absence of pinning agents such as impurities or second-phase particles. Controlled thermal treatment, particularly a moderate and consistent heating rate during calcination, further promotes isotropic boundary migration, preventing localized acceleration of specific grains. These conditions collectively suppress abnormal grain growth and ensure microstructural homogeneity, which is essential for optimizing mechanical integrity and functional performance in polycrystalline ceramic systems, including bioceramics derived from biogenic sources such as eggshell [72][73].

3.6. DRS-UV Analysis

The band gap energy of the multiphase nanoparticles material was analyzed using a DRS-UV), specifically a Cary 60 instrument. As shown in Fig. 4(c), the UV-vis analysis results were used to calculate the bandgap energy through the Tauc Plot method. As shown Fig. 4(d), the bandgap energy value obtained for multiphase nanoparticles 5.9578 eV. This suggests that calcination product showed insulating properties [74]. Furthermore, the UV-vis analysis results showed a significant absorption peak at 332 and 349 nm, suggesting the presence of crystal defects in calcined chicken eggshell powder. Crystal defects. and strain arising during pore formation often introduce structural imperfections that create energy levels within the band gap, thereby altering the material's optical and electronic properties. The defects reduced the purity of crystal phase, as shown by the observed variations in particle size from SEM and PSA analyses. The formation of electron-hole pairs due to crystal defects could alter the material's properties, leading to a more semiconductor-like behavior, which may enhance photocatalytic activity and influence charge carrier dynamics in energy-related applications [75]–[77].

The wide bandgap of 5.96 eV confirms the

Table 5. Descriptive statistics of antibacterial activity.

Parameters	Multiphase nanoparticles 20 µg/disk*	Positive control SAM 20**
Number of replicates	6	1
Positive response rate	3/6 (50%)	1/1 (100%)
Mean inhibition zone ± SD	10.06 ± 0.02 mm	23.04 mm
Median (entire dataset)	5.02 mm	23.04 mm
Data range	0 – 10.08 mm	-
Activity category	Weak - Intermediate	Strong

* (n = 6); ** (n = 1)

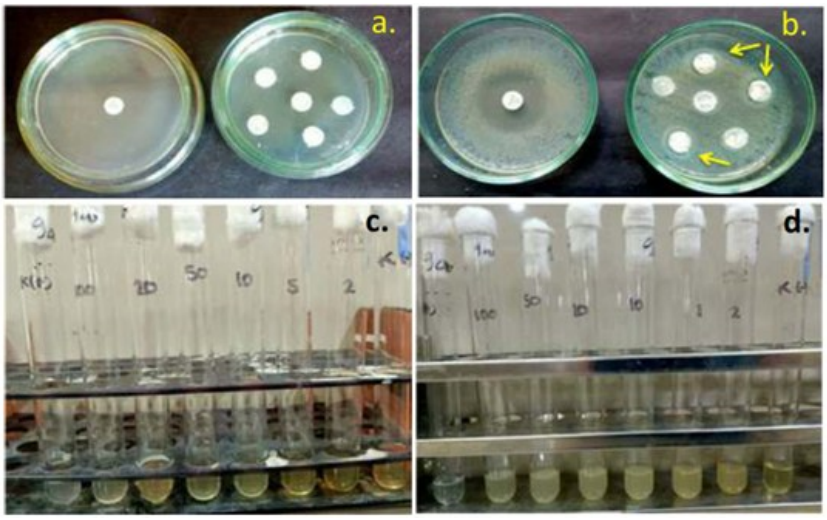

Figure 7. Antibacterial assays of multiphase nanoparticles against ECC (cf. *Enterobacter hormaechei*), (a) Disk diffusion setup pre-incubation: SAM 20 control (n = 1, left), and nanoparticle disks (n = 6, right). (b) Post-incubation results: inhibition zones measured for descriptive statistical analysis, (c) MIC assay setup pre-incubation: serial nanoparticle dilutions in broth. (d) Post-incubation MIC results: turbidity in all tubes indicates bacterial growth at all tested concentrations (MIC > maximum concentration evaluated).

insulating nature of themultiphase nanoparticles, indicating that it is not photoactive under natural light not photoactive under natural sunlight, which predominantly consists of photons with energies ≤3.1 eV (corresponding to wavelengths ≥400 nm) [70][78]. Therefore, any observed antibacterial activity is not due to photocatalysis, but likely stems from the release of Ca^{2+} and OH^- ions, which can disrupt bacterial membranes and create an alkaline microenvironment hostile to microbial growth. Thus, the bandgap value primarily reflects the material's electronic structure, not its antibacterial mechanism [59].

3.7. Isolation, Identification, and Pathogenicity Testing

Fig. 4(a) is the result of Gram staining of bacteria grown in nutrient broth culture. The results show that there are three bacteria morphology, namely short Gram-negative rods, long Gram-negative rods, and long Gram-positive rods. Furthermore, Fig. 4(b) provides information on the characteristics of bacteria colonies in MacKonkey agar culture, namely the first colony is irregular, pink, large, serrated, and convex. The second colony is round, pink, medium, flat, and convex, while the third is round, pink, small, flat, and convex. Fig. 4(c) and 4(d) show characteristics of bacteria colonies in NAP culture which appear to produce yellow pigments, showing the presence of suspect bacteria [79].

As previously mentioned, the initial hypothesis of this study was that the bacterial isolate belonged to Xoo; therefore, identification was performed using PCR with species-specific primers. However, PCR analysis yielded no detectable amplicon corresponding to Xoo, leading to the conclusion that this isolate is not Xoo. Consequently, identification was further pursued through 16S rRNA gene sequencing. The 16S rRNA gene is highly conserved, universally present in all prokaryotes, and evolves at a slow rate [80], making it a reliable molecular marker for taxonomic classification and phylogenetic inference at the genus and species levels.

This molecular marker enables reliable genus-level identification, especially when phenotypic traits are ambiguous. Comparative alignment against curated databases by NCBI, ensures precise taxonomic assignment. Given the isolate's atypical PCR result, 16S rRNA sequencing provides a hypothesis-free method to determine its identity. The sequence will undergo basic local alignment search tool (BLAST) analysis to identify closest relatives, followed by phylogenetic tree construction. The hypervariable regions within the 16S rRNA gene enable differentiation at the species level [81]. As indicated in Table 3, the DNA

template used for 16S rRNA gene amplification via PCR exhibited a concentration of 177.9 ng/μL and high purity ratios (A260/280 ≈ 1.93; A260/230 ≈ 2.23). These values indicate that the template DNA is of high quality, thereby ensuring the accuracy and reliability of subsequent sequencing results.

Fig. 5(a) presents the agarose gel electrophoresis results, demonstrating both the quality of the DNA template used and the integrity of the PCR-amplified products. A distinct, well-defined band is visible in both the test sample and the positive control, while no amplification is observed in the negative control confirming the specificity and absence of contamination in the reaction. The PCR amplification of the 16S rRNA gene yielded a DNA fragment of 1,394 bp in length, which corresponds closely to the expected size for bacterial 16S rRNA genes (~1,500 bp) [82]. This slight deviation may reflect primer binding site variation or partial gene amplification but remains within acceptable limits for downstream sequencing. The high yield and purity confirm optimal PCR conditions, ensuring reliable taxonomic resolution in subsequent phylogenetic analyses.

The PCR amplification of the 16S rRNA gene yielded a DNA fragment of 1,394 bp in length, which corresponds closely to the expected size for bacterial 16S rRNA genes (~1,500 bp) [83]. This slight deviation may reflect primer binding site variation or partial gene amplification but remains within acceptable limits for downstream sequencing. The high yield and purity confirm optimal PCR conditions, ensuring reliable taxonomic resolution in subsequent phylogenetic analyses. This finding, the high fidelity and appropriate size of the 16S rRNA amplicon underscore its suitability for accurate phylogenetic classification, thereby providing a robust molecular foundation for the taxonomic identification of the target Gram-negative isolate and its contextualization among known plant-pathogenic bacteria. within *Xanthomonadaceae*, 16S rRNA conservation enables genus-level but not species-level identification.

Table 4 presents the BLAST analysis results of the 16S rRNA sequence from the "Djayasinga" isolate. Among the top 10 matches, all hits correspond to the genus *Enterobacter.* The highest sequence identity (99.86%) was observed with *Enterobacter hormaechei* strain K-9 (accession no. OR708652.1), as well as other strains such as FF26 and FF20. The high percent identity (≥99.7%) strongly supports the classification of this isolate as closely related to *Enterobacter hormaechei.* According to established taxonomic thresholds, a 16S rRNA sequence similarity of ≥97.5% is generally considered indicative of species-level identity [83][84].

However, for definitive species identification, additional genomic or phenotypic analyses (e.g., whole-genome sequencing or multilocus sequence typing) are recommended, as 16S rRNA gene similarity alone may not resolve closely related species within the genus *Enterobacter*. These results strongly suggest that the "Djayasinga" isolate can be classified as ECC (cf. *Enterobacter hormaechei*). To the best of our knowledge, this is the first report indicating that members of the genus *Enterobacter* are associated with bacterial leaf blight in rice plants in Indonesia. The initial hypothesis that the isolate belongs to *Xanthomonas oryzae* was tested by restricting BLAST searches to *Xanthomonas oryzae* sequences; however, the maximum sequence identity obtained was only ~92.6% with *Xanthomonas. oryzae pv. oryzae* (query cover ≤97%). This value falls significantly below the established species-level identity threshold, confirming that the "Djayasinga" isolate does not belong to the genus *Xanthomonas* (Fig. 5).

Further pathogenicity testing following Koch's

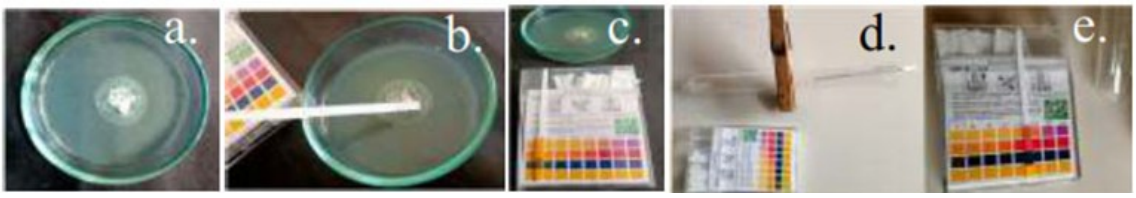

Figure 8. (a) Inhibition zones on MHA cultures; (b, c) pH measurements within the inhibition zones; (d, e) pH measurements of the multiphase nanoparticles material.

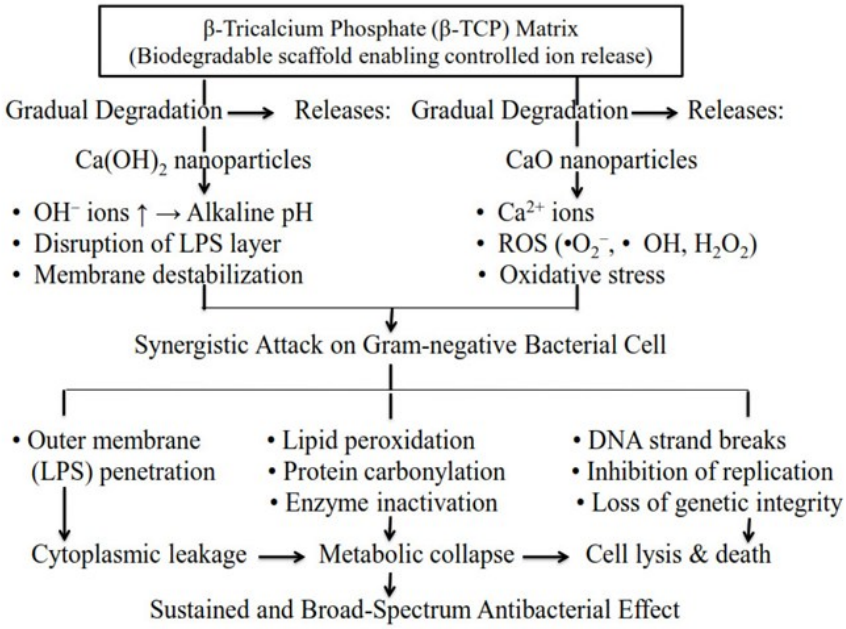

Figure 9. Diagram Schematic illustration of multiphase nanoparticles for sustained antibacterial ion release.

postulates are required to confirm the causal role of this isolate in rice leaf blight symptoms. The phylogenetic tree places the "Djayasinga" isolate within a well-supported clade alongside ECC, and in close proximity to *Enterobacter cloacae* DSM 30054, reflecting its placement within the *Enterobacter cloacae* complex (Fig. 4(b)). Members of the ECC are notoriously difficult to distinguish based solely on 16S rRNA gene sequences due to their high intra-complex genetic similarity [84]. Consequently, accurate species delineation within the Enterobacter cloacae complex necessitates complementary approaches such as multilocus sequence analysis (MLSA), whole-genome sequencing, or phenotypic profiling. These integrative methods overcome the limited resolution of 16S rRNA sequencing and are essential for reliable identification, ecological interpretation, and assessment of potential pathogenicity in plant-associated isolates [85].

Pathogenicity testing confirmed that the bacterial isolate, identified via 16S rRNA gene amplification, fulfilled the criteria as the causal agent of bacterial blight in rice, consistent with modern Koch's postulates. Characteristic symptoms manifested as progressive chlorosis originating from the leaf margins and expanding into the lamina over a 6-day period post-inoculation (Fig. 4(e) – 4(f)). These symptoms align with the pathogenicity mechanisms of Gram-negative bacteria, involving chlorophyll metabolism disruption and oxidative stress induction in plant tissues [86].

In contrast, the negative control treatment using *E. coli* exhibited no yellow chlorosis; instead, local black necrosis was observed at the inoculation sites (Fig. 4(g) – 4(h)). This distinct pathological response indicates that the specific chlorotic symptoms in the test treatment were not attributable to mechanical wounding effects or a general response to foreign microbes, but rather resulted from a specific interaction between the isolate's virulence and the rice plant's physiological susceptibility. The necrotic phenotype observed in the *E. coli* control likely reflects a plant defense response involving programmed cell death (hypersensitive response) against a non-pathogenic microbe, as reported in incompatible plant-microbe interactions [87].

3.8. Antibacterial Activity Assay

In Fig. 6(a), the yellow arrow indicates the localization of the multiphase nanoparticle material on bacteria inoculated onto MHA culture medium. Subsequently, Fig. 6(b), marked with a red arrow, shows the formation of an inhibition zone around the multiphase nanoparticle material. Subsequently, bacteria from Fig. 6(b) were examined SEM, yielding Fig. 6(c), in which the blue circle delineates viable bacteria exhibiting a tendency to form clustered rod-shaped aggregates

originating from the region outside the inhibition zone.

In contrast, Fig. 6(d) highlighted by the black circle reveals rod-shaped bacteria that appear more dispersed, and display significant morphological alterations, including cellular swelling, indicative of structural damage. Based on the morphological differences between bacterial cells in Fig. 6(c) and 6(d), the observed cellular damage within the inhibition zones is strongly attributed to extreme alkalinity (pH ~12) mediated by OH^- ion release from the $Ca(OH)_2$ and CaO matrix. The resulting alkaline microenvironment can disrupt bacterial membrane integrity, denature proteins, and inhibit essential enzymatic activities, ultimately leading to cell death [88]. Ca^{2+} ions are documented to stabilize Gram-negative outer membranes via LPS bridging. Thus, Ca^{2+} release and reactive oxygen species (ROS) generation from CaO are considered secondary mechanisms reinforcing the biosidal effect, rather than serving as primary drivers. The specific Ca^{2+} warrants further inverstigation through Ca^{2+} modulation experiments or pH-mathced controls in future studies [89].

The antibacterial activity of multiphase nanoparticles against ECC was evaluated using disk diffusion and broth microdilution assays. As informed in Table 5, In the disk diffusion assay, disks impregnated with nanoparticles (20 µg/disk, n = 6) were prepared alongside a positive control (SAM 20, n = 1) (see Fig. 7(a)). Post-incubation observations revealed variable inhibition zones around the nanoparticle disks (Fig. 7(b)), with descriptive analysis indicating a response rate of 50% (3 out of 6 replicates). Among the positive replicates, the mean inhibition zone was 10.06 ± 0.02 mm, whereas the median for the entire dataset was 5.02 mm (range: 0–10.08 mm). In comparison, the positive control yielded a consistent inhibition zone of 23.04 mm, confirming the susceptibility of ECC.

For the MIC assay, serial dilutions of multiphase nanoparticles (2–100 µg/mL) were prepared in BHIB media (Fig. 7(c)). Post-incubation results showed uniform turbidity across all test tubes containing nanoparticle dilutions (Fig. 7(d)), indicating bacterial growth at all tested concentrations (MIC > 100 µg/mL). Positive and negative controls validated the assay conditions. The synthesized multiphase nanoparticles exhibited limited antibacterial potential against ECC, with the mean inhibition zone of positive replicates reaching approximately 44% of the standard antibiotic control (SAM 20). However, the inconsistent activity observed (50% response rate; Fig. 7(b)) likely reflects the limited diffusion properties of insoluble calcium-based nanoparticles within the agar media. Unlike soluble antibiotics that diffuse

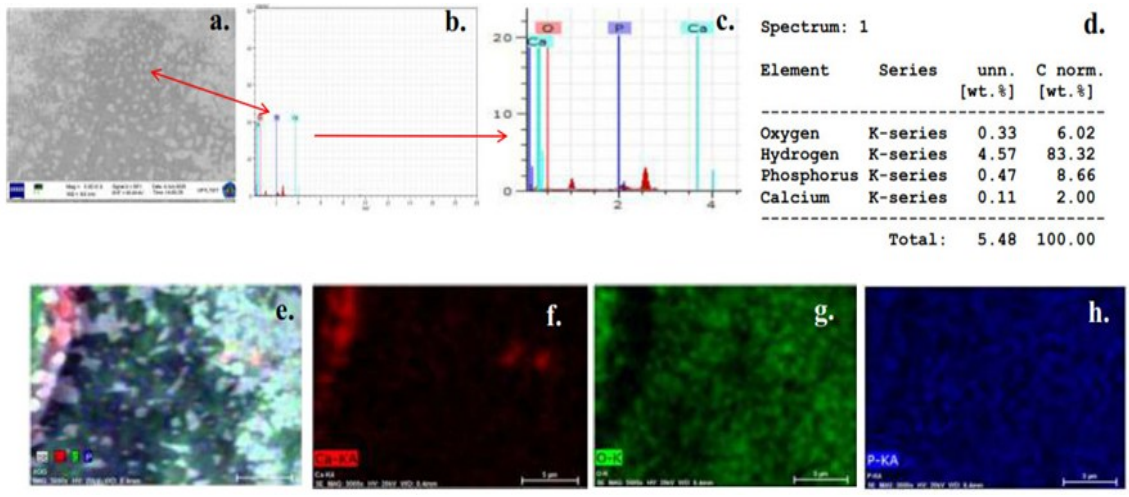

Figure 10. SEM–EDS analysis of calcium-rich multiphase nanoparticles against ECC (cf. *E. hormaechei)*, (a) SEM image showing nanoparticle-induced damage with EDS point analysis; (b,c) magnified regions linked to (a); (d) EDS spectrum from a single treated cell; (e–h) EDS elemental maps showing spatial distribution of Ca. and other elements on cells from the inhibition zone.

readily, bioactive ions (Ca^{2+}, OH^-) from the eggshell-derived matrix require gradual dissolution, potentially resulting in heterogeneous distribution at the disk-agar interface [90]. This diffusion limitation is further supported by the MIC assay results, where turbidity across all dilutions (Fig. 7 (d)) indicated no inhibitory effect within the tested concentration range (MIC > 100 µg/mL). The discrepancy between disk diffusion (partial activity), and MIC (no activity) suggests that the highly localized concentration of nanoparticles at the disk-agar interface may allow for limited ion release, whereas dispersed concentrations in broth (2–100 µg/mL) were insufficient to achieve a bacteriostatic effect. These findings indicate that although the material possesses inherent antibacterial properties, its efficacy is constrained by solubility and dispersion factors. Future optimization of particle dispersion, surface functionalization, or alternative delivery methods may be required to enhance reproducibility and potential for clinical applications [91].

Subsequently, pH measurements of the MHA culture medium before and after bacterial inoculation revealed a shift toward alkaline conditions, with the pH increasing from 7 to 8. In contrast, the multiphase nanoparticles material exhibited a markedly higher alkalinity, with a pH of 12, as previously shown in Fig. 8. This alkaline shift in the bacterial culture medium following nanoparticle exposure suggests the release of basic species particularly OH^- ions from the nanoparticle matrix into the surrounding environment [92]. Such pH elevation is a well-documented antibacterial mechanism of calcium-based nanomaterials (e.g., CaO and $Ca(OH)_2$), as it can disrupt bacterial membrane integrity, denature proteins, and interfere with essential enzymatic activities, ultimately leading to cell death.

The sustained alkaline microenvironment likely contributes significantly to the observed antibacterial efficacy against Gram-negative pathogens, reinforcing the role of pH modulation as a key factor in the bioactivity of eggshell-derived multiphase nanoparticles [93].

Fig. 9 presents a schematic illustration of the multiphase nanoparticles, conceptually summarizing the interconnected mechanisms underlying sustained antibacterial ion release. Specifically, β-TCP serves as a structural matrix for $Ca(OH)_2$, and CaO nanoparticles, enabling sustained ion release during biodegradation and thereby supporting prolonged antibacterial activity, primarily via OH^- delivery [94]. $Ca(OH)_2$ nanoparticles elevate the local pH, compromising the integrity of both the outer and cytoplasmic membranes of Gram-negative bacteria and destabilizing periplasmic proteins. Their nanoscale dimensions further facilitate penetration through porins in the lipopolysaccharide layer, enhancing antimicrobial efficacy. Meanwhile, CaO nanoparticles exert bactericidal effects through Ca^{2+} release and the generation of reactive oxygen species (ROS), which induce oxidative damage to membrane lipids, proteins, and bacterial DNA, ultimately triggering cell lysis [59][95]. Collectively, the antibacterial action of multiphase nanoparticles mediated through sustained Ca^{2+} and OH^- release, localized alkalization, and secondary oxidative stress demonstrates efficacy comparable to or potentially advantageous over other green-synthesized metal oxide nanomaterials [96]. For instance, ZnO nanoparticles typically rely on Zn^{2+} dissolution and ROS generation to inhibit phytopathogens such as *Xanthomonas spp*, yet their activity can be pH-sensitive and less persistent in neutral environments [97]. In contrast, the pH-buffering capacity and ion-release kinetics of Ca-based phases offer enhanced stability and prolonged antimicrobial activity under diverse environmental conditions.

As shown in Fig. 10(a) – 10(d), the SEM-EDS spectra and corresponding elemental mapping of bacterial cells reveal the presence of trace elements originating from the multiphase nanoparticle material, with the following atomic percentages: oxygen (6.02%), hydrogen (83.32%), phosphorus (8.66%), and calcium (2.00%). These results confirm the incorporation of key constituents of the multiphase nanoparticles into the bacterial cell environment. This information is relevant to the analysis result using the XRD method, which identifies the presence of multiphase nanoparticles in the form of crystal phases such as $Ca(OH)_2$, CaO, and β-TCP.

Fig. 10(e) – 10(h) indicates a stratified structure or tiered distribution of these elements within nanoparticles multiphase. Calcium occupying a

lower position likely indicates that calcium acts as a basic matrix or a deeper part of the material structure (Fig. 10(f)), while oxygen is distributed more widely, indicating that oxygen is an element closely related to various components in nanoparticles multiphase (Fig. 10(g)). Phosphate, which is more concentrated in the upper part, may indicate the presence of mineral phosphate deposits or accumulation on the surface or in certain layers (Fig. 10(h)). Furthermore, hydrogen (H) could not be detected using EDS instrument because the atomic number is low. The characteristic X-rays emitted by hydrogen are below the detection limit of the SEM-EDS Mapping system [98]. Through FTIR analysis, hydrogen was confirmed as the OH group at wavenumber of 3637 cm^{-1}, also XRD analysis showed the crystal phase of $Ca(OH)_2$, and the hexagonal shape of $Ca(OH)_2$ from the TEM analysis results.

4. CONCLUSIONS

This study successfully synthesized and characterized multiphase nanoparticles derived from chicken eggshell waste through a stepwise calcination process. Quantitative Rietveld refinement of XRD data confirmed the presence of three crystalline phases: $Ca(OH)_2$ (57.25 ± 1.2 wt%), CaO (10.34 ± 0.8 wt%), and β-tricalcium phosphate (β-TCP, 4.70 ± 0.5 wt%). The remaining ~27.71 wt% is attributed to amorphous content and/or minor crystalline phases below the detection limit of XRD (~2-5 wt%). This amorphous fraction is consistent with the mechanical-thermal decomposition synthesis route, which can generate non-crystalline calcium carbonate residues or disordered surface layers on nanoparticle surfaces. The crystalline phases exhibited nanoscale dimensions of 11–31 nm (XRD) and 20–23 nm (TEM), alongside agglomerated particle distributions ranging from 175 to 289 nm (PSA). Comprehensive structural (XRD, TEM, SEM), optical (UV-DRS, bandgap: 5.96 eV), and functional (FTIR, EDS) characterizations confirmed the presence of O-H, Ca-O, and PO_4^{3-} functional groups, which contribute to the material's structural stability and bioactivity. Consequently, this sustainable nanomaterial offers a viable solution for environmentally friendly agricultural disease management strategies implemented across diverse farming regions worldwide. The multiphase nanoparticles demonstrated antibacterial potential against bacterial isolates associated with rice leaf blight symptoms in Lampung, identified via 16S rRNA sequencing and BLAST analysis as *Enterobacter Cloacae* Complex (ECC) (cf. *E. hormaechei*) with 99.86% identity, rather than *Xanthomonas oryzae* as initially presumed. The antibacterial mechanism is primarily attributed to OH^--mediated alkalinity (pH ~12), which disrupts bacterial cell membranes and induces oxidative stress, as evidenced by morphological alterations observed within inhibition zones. The contribution of Ca^{2+} release is considered secondary, consistent with the documented membrane-stabilizing role of divalent cations in Gram-negative bacteria. The spatially graded distribution of Ca, O, and P elements (EDS mapping), coupled with the role of β-TCP as a potential controlled ion-release matrix, further reinforces the potential of this material as a sustainable antibacterial agent for eco-friendly agricultural applications. Future studies employing whole-genome sequencing, and pH-matched controls are recommended to further delineate species-level taxonomy and mechanistic pathways.

AUTHOR INFORMATION

Corresponding Author

Rudy Tahan Mangapul Situmeang — Department of Chemistry, University of Lampung, Bandar Lampung-35145 (Indonesia);
orcid.org/0000-0001-6622-0362
Email: rudy.tahan@fmipa.ac.id

Authors

Rodhiansyah Djayasinga — Doctoral program of Mathematics and Natural Science, University of Lampung, Bandar Lampung-35145 (Indonesia);
orcid.org/0000-0003-2089-0795

Wasinton Simanjuntak — Department of Chemistry, University of Lampung, Bandar Lampung-35145 (Indonesia);
orcid.org/0000-0001-8152-5084

Sumardi Sumardi — Department of Biology, University of Lampung, Bandar Lampung-35145 (Indonesia);

orcid.org/0000-0002-2773-7083
Sutopo Hadi — Department of Chemistry, University of Lampung, Bandar Lampung-35145 (Indonesia);
orcid.org/0000-0001-6464-7215
Mimi Sugiarti — Department of Medical Laboratory Technology, Poltekkes Kemenkes Tanjungkarang, Bandar Lampung-35145 (Indonesia);
orcid.org/0000-0001-5138-3687
Hartanti Hartanti — Department of Medical Laboratory Technology, Poltekkes Kemenkes Tanjungkarang, Bandar Lampung-35145 (Indonesia);
orcid.org/0000-0003-3551-7045

Author Contributions

Conceptualization, Methodology, Software, Formal Analysis, Investigation, Resources, Data Curation, Visualization, Funding Acquisition, Project Administration, and Writing – Original Draft Preparation, R. D.; Validation, and Writing – Review & Editing R. D., R. T. M. S., H. H.; Supervision R. D., R. T. M. S., W. S., S. H., S. S., M. S., H. H.

Conflicts of Interest

The authors declare no conflict of interest.

ACKNOWLEDGEMENT

The authors would like to express their deepest gratitude to the Ministry of Health of the Republic of Indonesia for providing funds and opportunities to conduct this research, as stipulated in the Decree of the Director General of Health Resources Number HK.02.03/F/2322/2023. Thanks to the Faculty of Mathematics and Natural Sciences, University of Lampung, which has provided enormous support so that this research can be completed properly.

DECLARATION OF GENERATIVE AI

We utilized Qwenlm artificial intelligence technology to discuss the reasons for the limitations of SEM-EDS mapping in detecting hydrogen elements from the performance of the materials we synthesized, and also AI Chatpdf to help analyze the pore size curve.

REFERENCES

[1] P. Yang, F. Li, S. Huang, M. Luo, W. Lin, G. Yuan, and Q. Li. (2020). "Physiological And Transcriptional Response Of Xanthomonas oryzae pv. oryzae To Berberine, An Emerging Chemical Control". *Phytopathology.* **110** (5): 1027-1038. 10.1094/PHYTO-09-19-0327-R.

[2] T. Boonsrangsom, A. Boondech, W. Chansongkram, N. Suachaowna, K. Buddhachat, T. Rungrat, J. Jumpathong, P. Pongcharoen, P. Inthima, N. Aeksiri, K. Ratanasut, and K. Sujipuli. (2025). "Molecular Characterization And Pathogenicity Of Xanthomonas oryzae pv. oryzae Isolates From Lower Northern Thailand, The Causal Agent Of Rice Bacterial Blight". *Physiological And Molecular Plant Pathology.* **136** : 102550. 10.1016/j.pmpp.2024.102550.

[3] Y. Tian, J. Luo, H. Wang, H. E. M. Zaki, S. Yu, X. Wang, T. Ahmed, M. S. Shahid, C. Yan, J. Chen, and B. Li. (2022). "Bioinspired Green Synthesis Of Silver Nanoparticles Using Three Plant Extracts And Their Antibacterial Activity Against Rice Bacterial Leaf Blight Pathogen Xanthomonas oryzae pv. oryzae". *Plants.* **11** (21): 2892. 10.3390/plants11212892.

[4] Y. Chen, T. Li, Z. Jin, and Y. R. Chi. (2022). "New Axially Chiral Molecular Scaffolds With Antibacterial Activities Against Xanthomonas oryzae pv. oryzae For Protection Of Rice". *Journal of Agricultural and Food Chemistry.* **70** (20): 6050-6058. 10.1021/acs.jafc.2c01407.

[5] M. Zhu, Y. Li, D. Chen, C. Li, G. Ouyang, and Z. Wang. (2023). "Allicin-Inspired Disulfide Derivatives Containing Quinazolin-4(3H)-One As A Bacteriostat Against Xanthomonas oryzae pv. oryzae". *Pest Management Science.* **79** (2): 537-547. 10.1002/ps.7221.

[6] J. Lai, W. Peng, S. Song, J. Jiang, and B. Liu. (2024). "Transcriptome Analysis Reveals The Inhibitory Mechanism Of 3,4-

Dimethoxyphenol From Streptomyces albidoflavus Strain ML27 Against Xanthomonas oryzae pv. oryzae". *Pesticide Biochemistry And Physiology.* **202** : 105913. 10.1016/j.pestbp.2024.105913.

[7] Q. Xie, G. Lao, Y. Fang, X. Gao, Z. Tan, W. Miao, and P. Jin. (2025). "Investigating Polyhydroxyalkanoate Synthesis For Insights Into Drug Resistance In Xanthomonas oryzae pv. oryzae". *International Journal of Molecular Sciences.* **26** (4): 1601. 10.3390/ijms26041601.

[8] H. B. Lee, J. P. Hong, and S. B. Kim. (2010). "First Report Of Leaf Blight Caused By Pantoea agglomerans On Rice In Korea". *Plant Disease.* **94** (11): 1372. 10.1094/PDIS-05-10-0374.

[9] K. K. Mondal, C. Mani, J. Singh, J. G. Kim, and M. B. Mudgett. (2011). "A New Leaf Blight Of Rice Caused By Pantoea ananatis In India". *Plant Disease.* **95** (12): 1582. 10.1094/PDIS-06-11-0533.

[10] Y. Xue, M. Hu, S. Chen, A. Hu, S. Li, H. Han, G. Lu, L. Zeng, and J. Zhou. (2021). "Enterobacter asburiae And Pantoea ananatis Causing Rice Bacterial Blight In China". *Plant Disease.* **105** (8): 2078-2088. 10.1094/PDIS-10-20-2292-RE.

[11] J. Rocha, L. R. Shapiro, S. Chimileski, and R. Kolter. (2024). "Complementary Roles Of EPS, T3SS And Expansin For Virulence Of Erwinia tracheiphila, The Causative Agent Of Cucurbit Wilt". *bioRxiv.* 10.1101/2024.06.24.600446.

[12] M. Zhang, S. Tang, C. Lin, Z. Lin, L. Zhang, W. Dong, and N. Zhong. (2025). "Hyperspectral Imaging And Machine Learning For Diagnosing Rice Bacterial Blight Symptoms Caused By Xanthomonas oryzae pv. oryzae, Pantoea ananatis And Enterobacter asburiae". *Plants.* **14** (5): 733. 10.3390/plants14050733.

[13] M. Chen, J. Wang, B. Liu, Y. Zhu, R. Xiao, W. Yang, C. Ge, and Z. Chen. (2020). "Biocontrol Of Tomato Bacterial Wilt By The New Strain Bacillus velezensis FJAT-46737 And Its Lipopeptides". *BMC Microbiology.* **20** (1): 160. 10.1186/s12866-020-01851-2.

[14] X. Zhao, H. Wang, X. Wang, and X. Zhao. (2024). "Sustainable Application Of Waste Eggshell As Fillers In Alkali-Activated Solid Waste-Based Materials: Varying Treated Methods And Particle Sizes". *Construction And Building Materials.* **425** : 136040. 10.1016/j.conbuildmat.2024.136040.

[15] A. Purnomo and R. Djayasinga. (2025). "Green Synthesis Of Ca(OH)2 Nanoparticles From Chicken Eggshell Waste As Antibacterial Agent". *International Journal Of Public Health Science.* **14** (2): 927. 10.11591/ijphs.v14i2.23869.

[16] A. Haleem, M. Javaid, R. P. Singh, S. Rab, and R. Suman. (2023). "Applications Of Nanotechnology In Medical Field: A Brief Review". *Global Health Journal.* **7** (2): 70-77. 10.1016/j.glohj.2023.02.008.

[17] M. B. Mobarak, M. N. Islam, F. Chowdhury, M. N. Uddin, M. S. Hossain, M. Mahmud, U. S. Akhtar, N. I. Tanvir, A. F. M. M. Rahman, and S. Ahmed. (2023). "Calcined Chicken Eggshell-Derived Biomimetic Nano-Hydroxyapatite As A Local Drug-Delivery Aid For Doxycycline Hyclate: Characterization, Bio-Activity, Cytotoxicity, Antibacterial Activity, And In Vitro Release Study". *RSC Advances.* **13** (51): 36209-36222. 10.1039/D3RA07010G.

[18] S. Kusumasari, M. A. Syabana, V. Y. Pamela, and B. Meindrawan. (2024). "Potential Use Of Food Waste In Food Processing To Add Nutritional Value". *E3S Web of Conferences.* **483** : 02006. 10.1051/e3sconf/202448302006.

[19] E. P. Bran, O. Patriciu, L. Grosu, I. Alexa, B. Bălănucă, A. Nicoară, and A. Fînaru. (2025). "The Influence Of Different Parameters For The Removal Of Pb And Zn Ions On Unmodified Waste Eggshells". *Materials.* **18** (12): 2794. 10.3390/ma18122794.

[20] F. S. Irwansyah, A. R. Noviyanti, D. R. Eddy, and R. Risdiana. (2022). "Green Template-Mediated Synthesis Of Biowaste Nano-Hydroxyapatite: A Systematic Literature Review". *Molecules.* **27** (17): 5586. 10.3390/molecules27175586.

[21] B. J. Madhu, H. Bhagyalakshmi, B. Shruthi, and M. Veerabhadraswamy. (2021).

"Structural, AC Conductivity, Dielectric And Catalytic Behavior Of Calcium Oxide Nanoparticles Derived From Waste Eggshells". *SN Applied Sciences.* **3** (6): 637. 10.1007/s42452-021-04607-3.

[22] L. Habte, N. Shiferaw, D. Mulatu, T. Thenepalli, R. Chilakala, and J. Ahn. (2019). "Synthesis Of Nano-Calcium Oxide From Waste Eggshell By Sol-Gel Method". *Sustainability.* **11** (11): 3196. 10.3390/su11113196.

[23] M. Minakshi, S. Higley, C. Baur, D. R. G. Mitchell, R. T. Jones, and M. Fichtner. (2019). "Calcined Chicken Eggshell Electrode For Battery And Supercapacitor Applications". *RSC Advances.* **9** (46): 26981-26995. 10.1039/C9RA04289J.

[24] M. E. S. Ismaiel Saraya and H. H. A. E. L. Rokbaa. (2017). "Formation And Stabilization Of Vaterite Calcium Carbonate By Using Natural Polysaccharide". *Advances In Nanoparticles.* **6** (4): 158-182. 10.4236/anp.2017.64014.

[25] N. Laohavisuti, B. Boonchom, W. Boonmee, K. Chaiseeda, and S. Seesanong. (2021). "Simple Recycling Of Biowaste Eggshells To Various Calcium Phosphates For Specific Industries". *Scientific Reports.* **11** (1): 15143. 10.1038/s41598-021-94643-1.

[26] N. C. Andrés, N. L. D'Elía, J. M. Ruso, A. E. Campelo, V. L. Massheimer, and P. V. Messina. (2017). "Manipulation Of Mg2+–Ca2+ Switch On The Development Of Bone Mimetic Hydroxyapatite". *ACS Applied Materials & Interfaces.* **9** (18): 15698-15710. 10.1021/acsami.7b02241.

[27] W. Cui, Q. Song, H. Su, Z. Yang, R. Yang, N. Li, and X. Zhang. (2020). "Synergistic Effects Of Mg-Substitution And Particle Size Of Chicken Eggshells On Hydrothermal Synthesis Of Biphasic Calcium Phosphate Nanocrystals". *Journal Of Materials Science & Technology.* **36** : 27-36. 10.1016/j.jmst.2019.04.038.

[28] R. Djayasinga, R. T. M. Situmeang, F. Unob, S. Hadi, P. Manurung, and S. Sumardi. (2024). "Chicken Eggshell Powder As Antibacterial Against Staphylococcus aureus And Escherichia coli Through In Vitro Studies". *Journal of Multidisciplinary Applied Natural Science.* **4** (1): 194-209. 10.47352/jmans.2774-3047.205.

[29] S. Sultana, M. S. Hossain, M. Mahmud, M. B. Mobarak, M. H. Kabir, N. Sharmin, and S. Ahmed. (2021). "UV-Assisted Synthesis Of Hydroxyapatite From Eggshells At Ambient Temperature: Cytotoxicity, Drug Delivery, And Bioactivity". *RSC Advances.* **11** (6): 3686-3694. 10.1039/D0RA09673C.

[30] V. H. Ingole, K. H. Hussein, A. A. Kashale, K. Ghule, T. Vuherer, V. Kokol, J. Chang, Y. Ling, A. Vinchurkar, H. N. Dhakal, and A. V. Ghule. (2017). "Ultrasound-Assisted Green Economic Synthesis Of Hydroxyapatite Nanoparticles Using Eggshell Biowaste And Study Of Mechanical And Biological Properties For Orthopedic Applications". *Journal Of Biomedical Materials Research Part A.* **105** (11): 2935-2947. 10.1002/jbm.a.36146.

[31] R. Djayasinga, A. Setiawan, A. Purnomo, A. Z. Amien, and H. Hartanti. (2022). "Utilization Of Breed Chicken Eggshells For Biodiesel Preparation From Waste Cooking Oil". *Journal of Multidisciplinary Applied Natural Science.* **2** (1): 41-46. 10.47352/jmans.2774-3047.90.

[32] V. J, R. Kannan, R. U. Sankareswari, R. Akila, and M. A. Pillai. (2017). "Characterization Of New Bacterial Leaf Blight Of Rice Caused By Pantoea stewartii subsp. indologenes In Southern Districts Of Tamil Nadu". *International Journal Of Environment, Agriculture And Biotechnology.* **2** (6): 3279-3284. 10.22161/ijeab/2.6.64.

[33] A. Raghunandana, D. Pramesh, G. Sunkad, C. Amoghavarsha, M. K. Yadav, U. Ngangkham, H. Pushpa, M. Prasannakumar, B. Raghavendra, H. R. Naik, S. E. Manjunatha, and S. Yenjerappa. (2023). "Genetic Diversity And Pathotype Profiling Of Xanthomonas oryzae pv. oryzae Isolates From Diverse Rice Growing Ecosystems Of Karnataka State Of India". *Plant Protection Science.* **59** (1): 31-47. 10.17221/76/2022-PPS.

[34] L. Jain, V. Kumar, S. K. Jain, P. Kaushal,

and P. K. Ghosh. (2023). "Isolation Of Bacteriophages Infecting Xanthomonas oryzae pv. oryzae And Genomic Characterization Of Novel Phage vB_XooS_NR08 For Biocontrol Of Bacterial Leaf Blight Of Rice". *Frontiers in Microbiology.* **14**. 10.3389/fmicb.2023.1084025.

[35] A. Asysyuura, A. A. Nawangsih, K. H. Mutaqin, and S. Sudir. (2017). "Identifikasi Patotipe Xanthomonas oryzae pv. oryzae Dari Tanaman Padi Di Sulawesi Selatan". *Jurnal Fitopatologi Indonesia.* **13** (3): 73. 10.14692/jfi.13.3.73.

[36] M. I. Baharuddin, S. N. Kamarul Baharin, A. E. Rak, and R. Hanaphi. (2020). "Isolation And Identification Of Bacteria From Phytoremediation Plant Of Heliconia psittacorum". *IOP Conference Series: Earth and Environmental Science.* **549** (1): 012069. 10.1088/1755-1315/549/1/012069.

[37] J. Tugume, C. Osundwa, G. Tusiime, C. Mukankusi, A. Ssekamate, P. Wasswa, and R. Buruchara. (2020). "Pathogenicity And Virulence Of Ugandan Isolates Of Common Bacterial Blight Disease Pathogen". *African Crop Science Journal.* **28** (2): 213-226. 10.4314/acsj.v28i2.7.

[38] C. Pang, L. Jin, H. Zang, D. S. S. Koklannou, J. Sun, J. Yang, Y. Wang, L. Xu, C. Gu, Y. Sun, X. Chen, and Y. Chen. (2024). "Establishment Of A System For Screening And Identification Of Novel Bactericide Targets In The Plant Pathogenic Bacterium Xanthomonas oryzae pv. oryzae Using Tn-Seq And SPR". *Journal Of Integrative Agriculture.* **23** (5): 1580-1592. 10.1016/j.jia.2023.04.043.

[39] P. C. Y. Woo, P. K. L. Leung, K. W. Leung, and K. Y. Yuen. (2000). "Identification By 16S Ribosomal RNA Gene Sequencing Of An Enterobacteriaceae Species From A Bone Marrow Transplant Recipient". *Molecular Pathology.* **53** (4): 211-215. 10.1136/mp.53.4.211.

[40] N. Adachi and T. Oku. (2000). "PCR-Mediated Detection Of Xanthomonas oryzae pv. oryzae By Amplification Of The 16S-23S rDNA Spacer Region Sequence". *Journal Of General Plant Pathology.* **66** (4): 303-309. 10.1007/PL00012969.

[41] M. Hajialigol, N. Falahi Charkhabi, F. Shahryari, and S. Sarikhani. (2023). "Association Of Rahnella victoriana, Enterobacter hormaechei subsp. hoffmannii And Citrobacter braakii With Walnut Decline". *Scientific Reports.* **13** (1): 11286. 10.1038/s41598-023-38427-9.

[42] N. Kim, J. J. Kim, I. Kim, M. Mannaa, J. Park, J. Kim, H. Lee, S. Lee, D. Park, W. J. Sul, and Y. Seo. (2020). "Type VI Secretion Systems Of Plant-Pathogenic Burkholderia glumae BGR1 Play A Functionally Distinct Role In Interspecies Interactions And Virulence". *Molecular Plant Pathology.* **21** (8): 1055-1069. 10.1111/mpp.12966.

[43] H. Ng'ombe, C. C. Luchen, L. Bote, M. Kasonde, K. Musonda, K. K. Mwape, D. H. Kuntawala, S. Silwamba, M. Chibuye, K. Chibesa, N. Mbewe, S. Bosomprah, W. Khan, L. Liebenberg, T. De Oliveira, E. Wilkinson, M. J. Dorman, A. Coghlan, M. Simuyandi, R. Chilengi, C. Chisenga, and N. R. Thomson. (2025). "Genomic Analysis And Antimicrobial Resistance Of Vibrio cholerae Isolated During Zambia's 2023 Cholera Epidemic". *Microbial Genomics.* **11** (12): 10.1099/mgen.0.001566.

[44] M. Surya, S. Sampath, S. B. Vairamuthu, P. G. Sravanthy, B. Ramachandran, M. M. Al-Ansari, T. Asmelash, and M. Saravanan. (2024). "Aloe vera-Mediated Silver-Selenium Doped Fucoidan Nanocomposites Synthesis And Their Multi-Faceted Biological Evaluation Of Antimicrobial, Antioxidant, And Cytotoxicity Activity". *Materials Technology.* **39** (1): 10.1080/10667857.2024.2331899.

[45] S. Seyedmajidi, R. Rajabnia, and M. Seyedmajidi. (2018). "Evaluation Of Antibacterial Properties Of Hydroxyapatite/Bioactive Glass And Fluorapatite/Bioactive Glass Nanocomposite Foams As A Cellular Scaffold Of Bone Tissue". *Journal Of Laboratory Physicians.* **10** (3): 265-270. 10.4103/JLP.JLP_167_17.

[46] S. Elabed, A. K. Mohamed, H. Youssef, H. Abdelhamied, E. Mokhtar, W. M. Elshemey,

M. W. Shafaa, and A. Meselhi. (2025). "Integrated Experimental And Computational Study Reveals Enhanced Antimicrobial Efficacy Of Amoxicillin Loaded In Oleic Acid Nanoemulsion Against Multidrug-Resistant Salmonella typhimurium". *RSC Advances.* **15** (41): 34237-34256. 10.1039/D5RA05196G.

[47] S. Shinde, V. Folliero, A. Chianese, C. Zannella, A. De Filippis, L. Rosati, M. Prisco, A. Falanga, A. Mali, M. Galdiero, M. Galdiero, M. Galdiero, M. Galdiero, and G. Franci. (2021). "Synthesis Of Chitosan-Coated Silver Nanoparticle Bioconjugates And Their Antimicrobial Activity Against Multidrug-Resistant Bacteria". *Applied Sciences.* **11** (19): 9340. 10.3390/app11199340.

[48] H. Sitepu, B. H. O'Connor, and D. Li. (2005). "Comparative Evaluation Of The March And Generalized Spherical Harmonic Preferred Orientation Models Using X-Ray Diffraction Data For Molybdite And Calcite Powders". *Journal of Applied Crystallography.* **38** (1): 158-167. 10.1107/S0021889804031231.

[49] D. M. H. H. S. Gutowsky. (1962). "A Nuclear Magnetic Resonance Determination Of The Hydrogen Positions In Ca(OH)2". *American Mineralogist.* **47** (11-12): 1231-1251.

[50] M. C. Verbraeken, E. Suard, and J. T. S. Irvine. (2011). "Order And Disorder In Ca2ND0.90H0.10: A Structural And Thermal Study". *Journal Of Solid State Chemistry.* **184** (8): 2088-2096. 10.1016/j.jssc.2011.05.062.

[51] M. Yashima, A. Sakai, T. Kamiyama, and A. Hoshikawa. (2003). "Crystal Structure Analysis Of β-Tricalcium Phosphate Ca3 (PO4)2 By Neutron Powder Diffraction". *Journal Of Solid State Chemistry.* **175** (2): 272-277. 10.1016/S0022-4596(03)00279-2.

[52] B. Hunter. "Rietica For Windows Version 4.0".

[53] E. H. Kisi. (1994). "Rietveld Analysis Of Powder Diffraction Patterns". *Materials Forum.* **18** : 135-155.

[54] B. Costa, J. Carvalho, S. Gavinho, T. Vieira, J. C. Silva, P. I. P. Soares, M. A. Valente, S. Soreto, and M. Graça. (2024). "Preparation And Characterization Of Zinc Ferrite And Gadolinium Iron Garnet Composite For Biomagnetic Applications". *Materials.* **17** (12): 2949. 10.3390/ma17122949.

[55] H. Cheng, J. Wei, M. Liang, S. Dai, X. Liu, L. Ma, H. Wang, and F. Lai. (2021). "Calcium Glycerolate Catalyst Derived From Eggshell Waste For Cyclopentadecanolide Synthesis". *Frontiers in Chemistry.* **9**. 10.3389/fchem.2021.770247.

[56] Z. Helwani, M. Ramli, E. Saputra, Y. L. Putra, D. F. Simbolon, M. R. Othman, and R. Idroes. (2020). "Composite Catalyst Of Palm Mill Fly Ash-Supported Calcium Oxide Obtained From Eggshells For Transesterification Of Off-Grade Palm Oil". *Catalysts.* **10** (7): 724. 10.3390/catal10070724.

[57] O. Awogbemi, F. Inambao, and E. I. Onuh. (2020). "Modification And Characterization Of Chicken Eggshell For Possible Catalytic Applications". *Heliyon.* **6** (10): e05283. 10.1016/j.heliyon.2020.e05283.

[58] H. Zhou, S. Hou, M. Zhang, H. Chai, Y. Liu, S. B. Bhaduri, L. Yang, and L. Deng. (2016). "Synthesis Of β-TCP And CPP Containing Biphasic Calcium Phosphates By A Robust Technique". *Ceramics International.* **42** (9): 11032-11038. 10.1016/j.ceramint.2016.03.246.

[59] K. Adaikalam, S. Hussain, P. Anbu, A. Rajaram, I. Sivanesan, and H. S. Kim. (2024). "Eco-Friendly Facile Conversion Of Waste Eggshells Into CaO Nanoparticles For Environmental Applications". *Nanomaterials.* **14** (20): 1620. 10.3390/nano14201620.

[60] F. Ma and P. Liu. (2016). "Surface Modification Of β-TCP With Stearic Acid And Its Effects On β-TCP/PLLA Biodegradable Composite Nanofibers". *Journal Of Bone Reports & Recommendations.* **2** (1). 10.4172/2469-6684.100020.

[61] T. Ungár, G. Tichy, J. Gubicza, and R. J. Hellmig. (2005). "Correlation Between Subgrains And Coherently Scattering Domains". *Powder Diffraction.* **20** (4): 366-

375. 10.1154/1.2135313.

[62] H. H. T. Vu, M. D. Khan, R. Chilakala, T. Q. Lai, T. Thenepalli, J. W. Ahn, D. U. Park, and J. Kim. (2019). "Utilization Of Lime Mud Waste From Paper Mills For Efficient Phosphorus Removal". *Sustainability.* **11** (6): 1524. 10.3390/su11061524.

[63] H. K. Tchakouté, D. E. T. Mabah, C. H. Rüscher, E. Kamseu, F. Andreola, M. C. Bignozzi, and C. Leonelli. (2020). "Preparation Of Low-Cost Nano And Microcomposites From Chicken Eggshell, Nano-Silica And Rice Husk Ash, And Their Utilisations As Additives For Producing Geopolymer Cements". *Journal Of Asian Ceramic Societies.* **8** (1): 149-161. 10.1080/21870764.2020.1718860.

[64] M. H. Azarian and W. Sutapun. (2022). "Tuning Polymorphs Of Precipitated Calcium Carbonate From Discarded Eggshells: Effects Of Polyelectrolyte And Salt Concentration". *RSC Advances.* **12** (23): 14729-14739. 10.1039/D2RA01673G.

[65] J. L. Bishop, S. J. King, M. D. Lane, A. J. Brown, B. Lafuente, T. Hiroi, R. Roberts, G. A. Swayze, J. Lin, and M. S. Román. (2021). "Spectral Properties Of Anhydrous Carbonates And Nitrates". *Earth And Space Science.* **8** (10). 10.1029/2021EA001844.

[66] T. Witoon. (2011). "Characterization Of Calcium Oxide Derived From Waste Eggshell And Its Application As CO2 Sorbent". *Ceramics International.* **37** (8): 3291-3298. 10.1016/j.ceramint.2011.05.125.

[67] B. Chitrakar, M. Zhang, X. Zhang, and S. Devahastin. (2020). "Bioactive Dietary Fiber Powder From Asparagus Leaf By-Product: Effect Of Low-Temperature Ball Milling On Physico-Chemical, Functional And Microstructural Characteristics". *Powder Technology.* **366** : 275-282. 10.1016/j.powtec.2020.02.068.

[68] Y. H. Wang, F. X. Zhang, and Y. W. Liu. (2001). "The Influence Of Grain Size And Temperature On The Mechanical Deformation Of Nanocrystalline Materials: Molecular Dynamics Simulation". *Chinese Physics.* **10** (5): 407-412. 10.1088/1009-1963/10/5/309.

[69] A. D. Salman, J. Tatjána, M. A. Al-Mayyahi, R. I. Ibrahim, T. A. Abdullah, and E. H. Khader. (2020). "Improvement Of Mechanical Properties Of Oil Well Cement By Incorporating Nano-CaCO3 Prepared From Eggshell Waste". *IOP Conference Series: Materials Science and Engineering.* **765** (1): 012006. 10.1088/1757-899X/765/1/012006.

[70] J. Kröger, A. Jiménez-Solano, G. Savasci, V. W. H. Lau, V. Duppel, I. Moudrakovski, K. Küster, T. Scholz, A. Gouder, M. Schreiber, F. Podjaski, C. Ochsenfeld, and B. V. Lotsch. (2021). "Morphology Control In 2D Carbon Nitrides: Impact Of Particle Size On Optoelectronic Properties And Photocatalysis". *Advanced Functional Materials.* **31** (28). 10.1002/adfm.202102468.

[71] A. Z. M. Rus, N. M. Abdullah, and M. F. L. Abdullah. (2013). "Characterization And Treatment Of Titanium Dioxide Via Ultrasonic Process With Melastoma malabathricum As Sustainable Sensitizer For Photovoltaic Solar Cell". *Journal of Chemistry.* **2013**. 10.1155/2013/251741.

[72] H. Zhou, B. Zalatan, J. Stanescu, M. P. Harmer, J. M. Rickman, L. He, C. J. Marvel, and B. Y. Chen. (2025). "Learning To Predict Rare Events: The Case Of Abnormal Grain Growth". *npj Computational Materials.* **11** (1): 82. 10.1038/s41524-025-01530-8.

[73] H. Che, Y. Gao, J. Yang, S. Hong, L. Hao, L. Xu, S. Taimoor, A. W. Robertson, and Z. Sun. (2024). "Hafnia For Analog Memristor: Influence Of Stoichiometry And Crystalline Structure". *New Carbon Materials.* **39** (1): 131-141. 10.1016/S1872-5805(24)60837-1.

[74] S. Joseph, S. Thomas, J. Mohan, A. S. Kumar, S. T. Jayasree, S. Thomas, and N. Kalarikkal. (2021). "Theoretical Study On Tuning Band Gap And Electronic Properties Of Atomically Thin Nanostructured MoS2/Metal Cluster Heterostructures". *ACS Omega.* **6** (10): 6623-6628. 10.1021/acsomega.0c05274.

[75] L. H. Li, K. H. Xue, J. H. Yuan, G. Q. Mao, and X. Miao. (2022). "Hafnia For Analog Memristor: Influence Of Stoichiometry And

Crystalline Structure". *Physical Review Materials.* **6** (8): 084603. 10.1103/PhysRevMaterials.6.084603.

[76] S. Mahajan. (2000). "Defects In Semiconductors And Their Effects On Devices". *Acta Materialia.* **48** (1): 137-149. 10.1016/S1359-6454(99)00292-X.

[77] C. C. Uydur, O. Arikan, and O. Kalenderli. (2018). "The Effect Of Insulation Defects On Electric Field Distribution Of Power Cables". *2018 IEEE International Conference On High Voltage Engineering And Application (ICHVE*. 1-4. 10.1109/ICHVE.2018.8641936

[78] A. Fujishima, X. Zhang, and D. Tryk. (2008). "TiO2 Photocatalysis And Related Surface Phenomena". *Surface Science Reports.* **63** (12): 515-582. 10.1016/j.surfrep.2008.10.001.

[79] T. Amin, V. Gupta, A. Sharma, P. K. Rai, V. K. Razdan, S. K. Sharma, S. K. Singh, J. A. Lone, M. Yaqoob, B. Singh, and S. K. Gupta. (2023). "Distribution Of Xanthomonas oryzae pv. oryzae Pathotypes In Basmati-Rice-Growing Areas Of Jammu And Kashmir, India". *Agronomy.* **13** (3): 713. 10.3390/agronomy13030713.

[80] D. L. Church, L. Cerutti, A. Gürtler, T. Griener, A. Zelazny, and S. Emler. (2020). "Performance And Application Of 16S rRNA Gene Cycle Sequencing For Routine Identification Of Bacteria In The Clinical Microbiology Laboratory". *Clinical Microbiology Reviews.* **33** (4). 10.1128/CMR.00053-19.

[81] J. S. Johnson, D. J. Spakowicz, B. Hong, L. M. Petersen, P. Demkowicz, L. Chen, S. R. Leopold, B. M. Hanson, H. O. Agresta, M. Gerstein, E. Sodergren, and G. M. Weinstock. (2019). "Evaluation Of 16S rRNA Gene Sequencing For Species And Strain-Level Microbiome Analysis". *Nature Communications.* **10** (1): 5029. 10.1038/s41467-019-13036-1.

[82] E. Stackebrandt and B. M. Goebel. (1994). "Taxonomic Note: A Place For DNA-DNA Reassociation And 16S rRNA Sequence Analysis In The Present Species Definition In Bacteriology". *International Journal Of Systematic And Evolutionary Microbiology.* **44** (4): 846-849. 10.1099/00207713-44-4-846.

[83] J. M. Janda and S. L. Abbott. (2007). "16S rRNA Gene Sequencing For Bacterial Identification In The Diagnostic Laboratory: Pluses, Perils, And Pitfalls". *Journal Of Clinical Microbiology.* **45** (9): 2761-2764. 10.1128/JCM.01228-07.

[84] A. Godmer, Y. Benzerara, A. C. Normand, N. Veziris, S. Gallah, C. Eckert, P. Morand, R. Piarroux, and A. Aubry. (2021). "Revisiting Species Identification Within The Enterobacter cloacae Complex By Matrix-Assisted Laser Desorption Ionization-Time Of Flight Mass Spectrometry". *Microbiology Spectrum.* **9** (1). 10.1128/Spectrum.00661-21.

[85] G. Cho, M. Stein, G. Fiedler, E. O. Igbinosa, L. P. Koll, E. Brinks, J. Rathje, H. Neve, and C. M. Franz. (2021). "Polyphasic Study Of Antibiotic-Resistant Enterobacteria Isolated From Fresh Produce In Germany And Description Of Enterobacter vonholyi sp. nov. And Enterobacter dykesii sp. nov". *Systematic And Applied Microbiology.* **44** (1): 126174. 10.1016/j.syapm.2020.126174.

[86] X. Chen, Y. Zhou, W. Liang, Y. Zhou, L. Xie, F. Hou, B. Zheng, and J. Li. (2025). "Proteomic Analysis Of Rice Mutant Pir1 Reveals Molecular Mechanisms Triggering PCD And Conferring High Resistance To Bacterial Blight". *Frontiers In Plant Science.* **16**. 10.3389/fpls.2025.1652068.

[87] M. Kabbage, B. Williams, and M. B. Dickman. (2013). "Cell Death Control: The Interplay Of Apoptosis And Autophagy In The Pathogenicity Of Sclerotinia sclerotiorum". *PLOS Pathogens.* **9** (4): e1003287. 10.1371/journal.ppat.1003287.

[88] H. Yu, J. Sun, K. She, M. Lv, Y. Zhang, Y. Xiao, Y. Liu, C. Han, X. Xu, S. Yang, G. Wang, and G. Zang. (2023). "Sprayed PAA-CaO2 Nanoparticles Combined With Calcium Ions And Reactive Oxygen Species For Antibacterial And Wound Healing". *Regenerative Biomaterials.* **10**. 10.1093/rb/rbad071.

[89] M. Feng, Y. Fang, C. Ma, X. Duan, Y. Zhang, B. Han, H. Hu, L. Meng, F. Wang,

and J. Li. (2021). "Mechanistic Insight Into Royal Protein Inhibiting The Gram-Positive Bacteria". *Biomolecules.* **11** (1): 64. 10.3390/biom11010064.

[90] B. Şensoy Gün, R. Gurbanov, and B. Tunalı. (2025). "Biofilm-Inhibiting ZnO@Eggshell Nanocomposites: Green Synthesis, Characterization, And Biomedical Potential". *BioMetals.* **38** (5): 1447-1468. 10.1007/s10534-025-00711-8.

[91] Y. Wang, T. Wen, F. Mao, S. Yang, Q. Zhang, X. Fu, C. Zhai, and H. Zhang. (2025). "Engineering Copper And Copper-Based Materials For A Post-Antibiotic Era". *Frontiers in Bioengineering and Biotechnology.* **13**. 10.3389/fbioe.2025.1644362.

[92] K. Pugdee, A. Klaisiri, and P. Phumpatrakom. (2023). "The Viability Of Human Dental Pulp Cells And Apical Papilla Cells After Treatment With Conventional Calcium Hydroxide And Nanoparticulate Calcium Hydroxide At Various Concentrations". *The Saudi Dental Journal.* **35** (8): 1000-1006. 10.1016/j.sdentj.2023.08.001.

[93] A. U. Khan, T. Hussain, Abdullah, M. A. Khan, M. M. Almostafa, N. S. Younis, and G. Yahya. (2023). "Antibacterial And Antibiofilm Activity Of Ficus carica-Mediated Calcium Oxide (CaONPs) Phyto-Nanoparticles". *Molecules.* **28** (14): 5553. 10.3390/molecules28145553.

[94] J. Yuan, B. Wang, C. Han, X. Huang, H. Xiao, X. Lu, J. Lu, D. Zhang, F. Xue, and Y. Xie. (2020). "Rice Bagasse Extract-Based Green Synthesis Of Zinc Oxide Nanoparticles: Characterisation, Assessment Of Anti-Skin Cancer, Antibacterial And Antioxidant Properties". *Materials Science And Engineering: C.* **114** : 111037. 10.1016/j.msec.2020.111037.

[95] A. Elbehiry and A. Abalkhail. (2025). "Antimicrobial Nanoparticles Against Superbugs: Mechanistic Insights, Biomedical Applications And Translational Frontiers". *Pharmaceuticals.* **18** (8): 1195. 10.3390/ph18081195.

[96] A. Kumar, A. Kaur, M. V. Singh, Vinod, and S. Dhiman. (2025). "Rice Bagasse Extract-Based Green Synthesis Of Zinc Oxide Nanoparticles: Characterisation, Assessment Of Anti-Skin Cancer, Antibacterial And Antioxidant Properties". *Sustainable Chemistry For Climate Action.* **7** : 100118. 10.1016/j.scca.2025.100118.

[97] Y. Abdallah, S. O. Ogunyemi, J. Bi, F. Wang, X. Huang, X. Shi, J. Jiang, E. Ibrahim, M. Mohany, S. S. Al-Rejaie, C. Yan, and B. Li. (2024). "Nickel Oxide Nanoparticles: A New Generation Nanoparticles To Combat Bacteria Xanthomonas oryzae pv. oryzae And Enhance Rice Plant Growth". *Pesticide Biochemistry And Physiology.* **200** : 105807. 10.1016/j.pestbp.2024.105807.

[98] N. Stojilovic. (2012). "Why Can't We See Hydrogen In X-Ray Photoelectron Spectroscopy?". *Journal Of Chemical Education.* **89** (10): 1331-1332. 10.1021/ed300057j.